

A SYSTEMATIC SEARCH FOR DUAL AGNS IN MERGING GALAXIES (ASTRO-DARING): II: FIRST RESULTS FROM LONG-SLIT SPECTROSCOPIC OBSERVATIONS

YANG-WEI ZHANG^{1,3}, YANG HUANG^{2,5}, JIN-MING BAI^{1,4,5}, XIAO-WEI LIU^{2,5}, JIAN-GUO WANG¹, XIAO-BO DONG¹,

Draft version November 9, 2021

ABSTRACT

Building a large sample of kiloparsec (kpc)-scale dual active galactic nuclei (AGNs) amongst merging galaxies is of vital importance to understand the co-evolution between host galaxies and their central super massive black holes (SMBHs). Doing so, with just such a sample, we have developed an innovative method of systematically searching and identifying dual AGNs of amongst kpc scale merging galaxies and selected 222 candidates at redshifts ≤ 0.25 . All the selected candidates have FIRST radio detection and at least one of two cores previously revealed as AGN spectroscopically. We report the first results from A SysTematic seaRch fOr Dual Agns in meRgINg Galaxies (ASTRO-DARING), which consist of spatially resolved long-slit spectroscopic observations of 41 targets selected from our merging galaxies sample carried out between November 2014 and February 2017, using the Yunnan Faint Object Spectrograph and Camera (YFOSC) mounted on the 2.4 meter telescope in Lijiang of Yunnan Observatories. Of these 16 are likely dual AGNs and 15 are newly identified. The efficiency of ASTRO-DARING is thus nearly 40 per cent. With this method, we plan to build the first even sample of more than 50 dual AGNs constructed using a consistent approach. Further analysis of the dual AGN sample shall provide vital clues for understanding the co-evolution of galaxies and SMBHs.

Keywords: techniques: spectroscopic – galaxies: active – galaxies: nuclei – galaxies: mergers – galaxies: interactions – galaxies: co-evolution

1. INTRODUCTION

Galaxy merging plays an vital role for galaxy growth in the standard Λ CDM cosmology (e.g., Kauffmann & Haehnelt 2000; Di Matteo et al. 2005; Kormendy & Ho 2013). As essentially all massive galaxies are believed to host a central super massive black hole (SMBH; e.g., Kormendy & Richstone 1995; Richstone et al. 1998), one expects to find SMBH pairs in the merging galaxies (e.g., Begelman et al. 1980; Milosavljević & Merritt 2001). The merging would also trigger active galactic nuclei (AGN) activities when large amounts of gas fall into the central SMBHs via the gravitational interactions (e.g., Hopkins et al. 2008; Kocevski et al. 2012; Treister et al. 2012). In this scenario, dual AGNs are expected to form in merging galaxies (e.g., Koss et al. 2012; Satyapal et al. 2017).

For merging galaxies of projected separations smaller than 15 kpc (typical tidal radius of a galaxy), the gravitational interactions between the two merging galaxies become significant (e.g., Begelman et al. 1980; Volonteri et al. 2003). Identifying dual AGNs at this critical stage before final coalescence amongst gas-rich merging galaxies can provide vital information to investigate the co-evolution of SMBHs and their host galaxies (e.g., Colpi & Dotti 2011; Yu et al. 2011), for example, the underlying physics of the tight scaling relations between black hole mass (M_{BH}) and

large-scale properties of the host galaxy found from observations, especially the well-known relation between central BH mass and host galaxy bulge velocity dispersion (σ ; e.g., Ferrarese & Merritt 2000; Gebhardt et al. 2000; Häring & Rix 2004; Gültekin et al. 2009; Graham & Scott 2013; Kormendy & Ho 2013; McConnell & Ma 2013). While considered fundamental and supported by bona fide observational evidence, it is still not clear whether the $M_{\text{BH}}-\sigma$ relation is universal and followed by all types of galaxies including merging galaxies (e.g., Komossa & Xu 2007; Fu et al. 2011a; Savorgnan & Graham 2015). The previous studies indicate that the dual AGN systems may not follow the typical $M_{\text{BH}}-\sigma$ relation defined from isolated AGNs and thus can contribute scatter to this relation (e.g., Blecha et al. 2011; Fu et al. 2011a). The physical mechanisms connecting the growth of BH mass and the host galaxy are also not well understood (e.g., Ricci et al. 2017; Sheinin & López-Sánchez 2017). Other questions related include how the phenomenon of dual AGNs is triggered and how they evolve as in the merging progresses (e.g., Treister et al. 2012; Satyapal et al. 2017). Being the late stage products of galaxy merging, dual AGNs can clearly help address these fundamental questions (e.g., Kosec et al. 2017; Solanes et al. 2019).

To answer the above questions, a large sample of dual AGNs is required. However, the current number of identified dual AGNs is limited, with a total number of no more than 50 (see the compilation in Das et al. 2018 and Huang et al. 2021, in preparation; hereafter Paper I). These confirmed dual AGNs are identified by a variety of methods, such as X-ray observations (e.g., Komossa et al. 2003; Guainazzi et al. 2005; Hudson et al. 2006; Liu et al. 2013; Comerford et al. 2011, 2015; Koss et al. 2016; Ellison et al. 2017), or radio observations (e.g., Rodriguez et al. 2006; Fu et al. 2011b, 2015; Müller-Sánchez et al. 2015; Rubinur et al. 2017), or optical spectroscopy (e.g., Liu et al. 2010b; Liu et al. 2011; Shen et al. 2011; Huang et al. 2014).

¹ Yunnan Observatories, Chinese Academy of Sciences, Kunming, Yunnan 650011, People's Republic of China; zhangyangwei@ynao.ac.cn; baijinming@ynao.ac.cn

² South-Western Institute for Astronomy Research, Yunnan University, Kunming 650500, People's Republic of China; yanghuang@ynu.edu.cn; x.liu@ynu.edu.cn

³ University of Chinese Academy of Sciences, Beijing 100049, People's Republic of China

⁴ Key Laboratory for the Structure and Evolution of Celestial Objects, Chinese Academy of Sciences, Kunming 650011, People's Republic of China

⁵ Corresponding authors

In the past decades, several systematic methods have been developed for identifying dual AGNs. One of the most ambitious methods is finding dual AGNs from the double-peaked AGNs (DPAGNs). As a potential mechanism, binary/dual AGN with projected separations ranging from 100 pc to 10 kpc could contribute the DPAGNs (e.g., Zhou et al. 2004; Wang et al. 2009). Thanks to massive spectroscopic surveys, such as SDSS and DEEP2 Galaxy Survey, hundreds of DPAGNs have been spectroscopically selected (e.g., Gerke et al. 2007; Wang et al. 2009; Liu et al. 2010a; Smith et al. 2010; Rosario et al. 2011; Ge et al. 2012; Barrows et al. 2013; Shi et al. 2014; McGurk et al. 2015). However, spatially resolved longslit/integral-field spectroscopy (e.g., Liu et al. 2011; Shen et al. 2011; McGurk et al. 2011; Comerford et al. 2012) and high resolution imaging (e.g., Liu et al. 2013, Comerford et al. 2015, Müller-Sánchez et al. 2015) follow-up observations show that only 2 to 5 per cent of the DPAGNs are dual AGNs and most of DPAGNs are produced by gas kinematics related to a single AGN (e.g., rotating gas disks or biconical outflows from the narrow line region (NLR) of AGN; Comerford et al. 2011; Fu et al. 2011a, 2012; Shen et al. 2011; Smith et al. 2011; Smith et al. 2012; Gabányi et al. 2014; Nevin et al. 2016). Most recently, the systematic search for dual AGNs based on radio imaging (Fu et al. 2015) and mid-infrared color (Satyapal et al. 2014, 2017) has been proposed but the number of identified dual AGNs is still very limited (see Section 4 for more details).

It is a challenging task to build a homogeneous dual AGN sample for the purpose of studying the co-evolution of SMBHs and host galaxies. A more robust and efficient new method is clearly desirable. Inspired by previous studies (e.g., Hennawi et al. 2006, 2010; Ellison et al. 2011; Satyapal et al. 2014; Rubinur et al. 2019), we have developed an innovative method to systematically find and identify dual AGNs amongst kpc scale merging galaxies (see Section 2.1 and Paper I for more details). With this new method, a total of 222 targeted candidates (merging galaxies) have been selected. To reveal their dual AGN nature, we have embarked on an observational campaign, a systematic search for dual AGNs in merging galaxies (ASTRO-DARING for short), using spatially resolved long-slit and aperture spectroscopy.

In this work (hereafter Paper II), we present the first results of ASTRO-DARING from November 2014 to February 2017 using the YFOSC mounted on the 2.4 m telescope in Lijiang (LJT) of the Yunnan Observatories (YNAO). The observation and data reduction are described in Section 2. The results are presented in Section 3. In Section 4, we discuss the implications and potential applications of our current results. Finally, a summary is given in Section 5. Cosmological constants $H_0 = 70 \text{ km s}^{-1} \text{ Mpc}^{-1}$, $\Omega_m = 0.3$, and $\Omega_\Lambda = 0.7$ are adopted throughout the paper and all wavelengths are vacuum.

2. OBSERVATION & DATA REDUCTION

2.1. Sample Selection

As mentioned above, ASTRO-DARING proposes an efficient method to search and identify dual AGNs amongst merging galaxies. To do so, we first select galaxies that are potentially undergoing a merging process from the SDSS photometric catalog from DR9 (Ahn & et al. 2013): galaxies exhibiting two optical cores⁶ separated by less than $8''$

⁶ Both cores are classified as galaxy in SDSS DR9 (Ahn & et al. 2013).

Table 1
Instrumental setup

Grism	Spectral range Å	Dispersion nm/pix	Resolution _{1,8} (km s^{-1})	Resolution _{2,5} (km s^{-1})
G8	5100 – 9600	0.15	330 ± 20	–
G14	3600 – 7500	0.17	500 ± 40	–
G3	3400 – 9100	0.29	730 ± 60	970 ± 70

Notes: Resolution_{1,8}: Median Resolution of the instrumental broadening for a slit width of $1.8''$. Resolution_{2,5}: Median Resolution of the instrumental broadening for a slit width of $2.5''$. The instrumental broadening was measured from the arc lamp spectra.

and at least one optical core with SDSS fiber spectra from DR12/14 (Alam et al. 2015; Abolfathi et al. 2018). Secondly, the candidates are selected with at least one radio detection from the FIRST survey (Helfand, White & Becker 2015) in order to exclude physically unrelated pairs as merging galaxies⁷. Typically, enhanced radio radiation are expected from merge-driven star formations or starbursts (e.g., Sanders et al. 1988; Bell et al. 2006; Jooe et al. 2009; Robaina et al. 2009). Based on this, the requirement of radio detection can help remove the physically unrelated pairs from the merging galaxies to a certain extent. Finally, only systems with at least one core previously identified as an AGN with redshift $z < 0.25$ by analyzing the SDSS DR12/14 spectra (Pâris et al. 2017, 2018) are selected as dual AGN candidates. In this manner, a total of 222 dual AGN candidates ($z < 0.25$) are selected amongst the merging galaxies sample from SDSS catalog. We note that the current sample has a rough limiting magnitude of i band model magnitude ~ 19.5 -20 due to the redshift cut ($z < 0.25$), and the sample will miss dual AGN systems with radio radiation below the FIRST detection threshold (i.e., 1 mJy). More details about sample selection are described in Paper I.

2.2. Observations

To identify the candidates as real dual AGNs, we have carried out the ASTRO-DARING campaign to collect spatially resolved long-slit spectroscopic observations of the candidates. The 2D spatially resolved long-slit spectra allow one to explore the activity nature of the two cores in the merging system (e.g., Shen et al. 2011) and thus help us diagnose whether the observed target is a real dual AGN or not. The long-slit spectra are required to cover the emission lines of $H\beta$, $[\text{O III}] \lambda 5007$, $[\text{O I}] \lambda 6300$, $H\alpha$, $[\text{N II}] \lambda \lambda 6549, 6583$ and $[\text{S II}] \lambda \lambda 6717, 6731$ in optical band with resolving power $R > 300$ (corresponding to a velocity resolution $> 1000 \text{ km s}^{-1}$), thus enabling us to identify AGN by either measuring the Full Width at Half Maximum (FWHM) of the Balmer emission lines or using the classical Baldwin-Phillips-Terlevich (BPT, Baldwin et al. 1981) diagrams with emission line ratios.

All spectroscopic observations reported here were obtained with the YFOSC mounted on the LJT of the YNAO as part of the ASTRO-DARING campaign. YFOSC is a multi-mode instrument for both imaging and low/medium resolution spectroscopy, working at the Cassegrain focus (Fan et al. 2015). The CCD sensor is a $2\text{k} \times 4\text{k}$ back-illuminated deep depletion chip, with a pixel size of $13.5 \mu\text{m}$ that projects to 0.283 arcsec

⁷ The FIRST survey has already released the final catalogue (Helfand, White & Becker 2015) and presented definitive high-resolution 20 cm maps covering in total $10\,575 \text{ deg}^2$ sky area at 1.4 GHz, using the Very Large Array (VLA) with a detection sensitivity of 1 mJy.

Table 2
Observational log

Name	RA (J2000)	Dec (J2000)	Redshift	Sep0 (''/kpc)	Sep1 (''/kpc)	Grism	Slit width ('')	Observing date UT	Seeing ('')	PA ^a (°)	Exposure time (s)
First phase (15 sources)											
J0151−0245	01:51:07.74	−02:45:27.66	0.0479	5.3/5.0	5.1/4.9	G14	1.8	20141211	2.2	98.3	2500
						G14	1.8	20150207	2.6		3000
J0225−0824	02:25:11.63	−08:24:38.38	0.1099	5.6/11.3	5.7/11.4	G14	1.8	20141210	2.4	146.6	2246 ^b
						G8	1.8	20141211	1.7		2500×2
J0737+4651	07:37:44.10	+46:51:07.96	0.0951	1.6/2.9	1.7/3.0	G8	1.8	20141212	1.6	25.2	2500+2100
						G14	1.8	20150209	1.0		3000
J0933+2114	09:33:47.76	+21:14:36.41	0.1722	4.1/11.9	4.0/11.7	G8	1.8	20150210	0.9	52.9	3000
						G8	1.8	20150211	1.4		3000
J1010+0612	10:10:43.36	+06:12:01.42	0.0978	7.1/12.8	7.1/12.8	G8	1.8	20150212	1.3	61.0	2410 ^b
J1017+3448	10:17:56.75	+34:48:50.36	0.1440	5.4/11.7	5.4/11.7	G8	1.8	20150207	2.8	134.9	3000
						G8	1.8	20150208	1.8		3000
J1105+1957	11:05:44.45	+19:57:46.29	0.1043	3.8/7.3	3.7/7.1	G8	1.8	20150211	1.6	8.6	3000
						G8	1.8	20150228	1.9		3000
J1200+3147	12:00:41.39	+31:47:46.28	0.1161	5.7/12.1	5.7/12.1	G8	1.8	20150212	1.6	33.2	3000
J1201−0153	12:01:49.74	−01:53:27.55	0.0907	7.0/11.8	7.1/12.0	G8	1.8	20150211	2.0	143.2	1292 ^b
J1535+3455	15:35:02.26	+34:55:38.43	0.1307	5.3/12.3	5.4/12.6	G8	1.8	20150301	1.6	93.1	3000
J1633+4718	16:33:23.58	+47:18:58.95	0.1158	3.8/8.0	4.0/8.4	G8	1.8	20150301	1.4	175.6	3000
J2150−0052	21:50:24.70	−00:52:42.78	0.1108	5.4/11.0	5.5/11.1	G8	1.8	20141115	1.8	53.1	3000
						G14	1.8	20141115	1.8		3000
J2226+0143	22:26:21.65	+01:43:29.88	0.2231	2.6/9.3	2.5/9.0	G8	1.8	20151115	1.6	79.8	3000
						G14	1.8	20151115	1.6		2387 ^b
J2233+0332	22:33:36.41	+03:32:34.70	0.1064	3.6/7.0	3.7/7.2	G8	1.8	20141114	1.8	6.4	3000
						G14	1.8	20141114	2.0		3000
J2258−0115	22:58:10.01	−01:15:16.26	0.1170	3.4/7.1	3.4/7.1	G14	1.8	20141111	2.0	10.1	2700+3600
						G8	1.8	20141111	2.0		2545 ^b
Second phase (26 sources)											
J0101−0957	01:01:58.62	−09:57:50.57	0.1523	5.3/14.1	5.4/14.3	G3	1.8	20151105	2.0	52.2	2380 ^b
J0141−0105	01:41:56.81	−01:05:32.03	0.1392	6.0/14.7	5.9/14.5	G3	1.8	20151106	3.0	5.6	2700
J0157+1155	01:57:23.82	+11:55:47.61	0.0888	4.5/7.5	4.5/7.5	G3	2.5	20161202	1.7	154.4	3000
						G3	2.5	20161203	2.1		2500
J0204−0248	02:04:24.83	−02:48:41.27	0.0750	3.4/4.9	3.5/5.0	G3	1.8	20151130	2.1	75.6	2500
						G3	2.5	20161204	2.2		1217±2500
J0206−0441	02:06:28.41	−04:41:10.54	0.1364	5.5/13.2	5.4/13.0	G3	2.5	20161202	1.5	82.1	3600
J0217−0845	02:17:03.46	−08:45:19.08	0.1081	6.0/12.0	6.2/12.2	G3	2.5	20161203	2.1	59.0	3000+3000
J0251−0837	02:25:11.63	−08:24:38.38	0.1323	4.9/11.4	4.8/11.3	G3	2.5	20161202	1.7	7.8	3500
						G3	2.5	20170105	1.8		3000
J0750+3530	07:50:57.26	+35:30:37.67	0.1762	3.4/10.3	3.4/10.3	G3	2.5	20170204	2.1	141.8	3000
J0752+3419	07:52:21.86	+34:19:35.58	0.1400	3.3/8.1	3.1/7.6	G3	1.8	20151123	1.5	59.9	3800
						G3	1.8	20151220	1.7		3000
J0756+2340	07:56:21.00	+23:40:39.40	0.0742	6.8/9.6	6.8/9.6	G3	2.5	20161204	3.0	48.6	3000
J0758+2705	07:58:46.99	+27:05:15.61	0.0987	3.3/6.0	3.4/6.2	G3	1.8	20151124	1.3	73.8	3000
J0813+4941	08:13:47.49	+49:41:09.83	0.0942	3.3/5.8	3.4/5.9	G3	2.5	20170204	2.2	139.9	3000
						G3	2.5	20170205	2.0		3000
J0813+5529	08:13:26.77	+55:29:18.07	0.0796	5.9/8.8	5.9/8.8	G3	2.5	20161204	3.0	132.1	3000
J0832+0937	08:32:02.71	+09:37:59.17	0.0750	4.3/6.2	4.2/6.0	G3	2.5	20170206	2.7	178.9	2500
J0833+1532	08:33:55.49	+15:32:36.62	0.1516	4.5/11.9	4.5/11.9	G3	2.5	20170205	2.0	149.4	3000
J0848+3515	08:48:09.69	+35:15:32.12	0.0570	5.6/6.2	5.7/6.3	G3	2.5	20170205	2.5	66.8	3000
						G3	2.5	20170206	1.8		2500
J0907+5203	09:07:14.44	+52:03:43.40	0.0596	7.4/8.5	7.4/8.5	G3	2.5	20170206	2.1	11.4	2500
J1214+2931	12:14:18.25	+29:31:46.70	0.0633	6.7/8.2	6.7/8.2	G3	1.8	20160528	1.5	61.2	3200
J1645+2057	16:45:07.91	+20:57:59.43	0.1300	4.2/9.8	4.2/9.8	G3	1.8	20160519	2.0	155.1	3200
J2145+1144	21:45:30.39	+11:44:03.66	0.1122	3.8/7.8	3.7/7.6	G3	1.8	20151106	2.2	93.5	2200
J2206+0003	22:06:35.08	+00:03:23.16	0.0461	4.7/4.3	4.5/4.1	G3	1.8	20151126	1.4	156.9	2000+2200
						G3	1.8	20151209	1.9		2700
J2210+0945	22:10:58.06	+09:45:00.92	0.1170	4.7/9.9	4.5/9.5	G3	1.8	20151106	1.5	19.1	2500
J2239+0012	22:39:32.21	+00:12:46.36	0.1615	4.1/11.4	4.2/11.7	G3	1.8	20151125	1.4	178.8	3000
						G3	1.8	20161024	1.3		2700
J2252+0106	22:52:22.35	+01:06:59.98	0.0717	3.2/4.4	3.1/4.2	G3	1.8	20161024	1.5	126.2	2700
						G3	2.5	20161204	1.7		3000
J2314+0653	23:14:39.21	+06:53:12.97	0.0875	4.1/6.7	4.2/6.9	G3	1.8	20151128	1.3	157.5	2300
						G3	1.8	20161024	1.8		3000
J2320+0741	23:20:41.53	+07:41:48.24	0.1316	4.4/10.2	4.5/10.5	G3	1.8	20161024	1.3	106.1	3000
						G3	2.5	20161204	1.6		3000

Notes: Sep0: The separation of two cores from the SDSS image. Sep1: The separation of two cores from the 2D spectrum.

^a PA: Position angle of the slit on the sky, in degrees east of north.

^b The exposure times of the observations were originally set to be longer (e.g., 3000s), but were cut short due to problems of the telescope tracking.

Table 3
Fluxes of well detected emission lines

Name	$f_{H\beta}$	$f_{[O III] \lambda 4959}$	$f_{[O III] \lambda 5007}$	$f_{[O II] \lambda 6300}$	$f_{[N II] \lambda 6549}$	$f_{H\alpha}$	$f_{[N II] \lambda 6583}$	$f_{[S II] \lambda 6717}$	$f_{[S II] \lambda 6731}$
First phase (6 Dual AGNs)									
J0151-0245WN	75 ± 23	31 ± 11	128 ± 12	115 ± 12	85 ± 14	68 ± 12	231 ± 18	145 ± 17	120 ± 17
J0151-0245ES	76 ± 22	52 ± 15	153 ± 13	109 ± 15	213 ± 18	247 ± 18	445 ± 11	272 ± 14	164 ± 14
J0933+2114EN	131 ± 84	437 ± 59	1494 ± 59	106 ± 37	540 ± 137	1663 ± 140	1238 ± 124	414 ± 122	193 ± 93
J0933+2114WS	399 ± 33	382 ± 31	1192 ± 30	215 ± 44	254 ± 54	929 ± 68	609 ± 57	229 ± 52	137 ± 48
J1017+3448NW	313 ± 106	286 ± 100	976 ± 104	128 ± 52	365 ± 81	1115 ± 71	665 ± 59	283 ± 18	152 ± 15
J1017+3448SE	118 ± 52	309 ± 40	1191 ± 40	77 ± 38	226 ± 120	723 ± 142	570 ± 96	98 ± 44	89 ± 45
J1105+1957EN	197 ± 14	58 ± 15	195 ± 17	57 ± 8	376 ± 14	1221 ± 13	893 ± 11	268 ± 17	242 ± 15
J1105+1957WS	110 ± 11	51 ± 19	230 ± 21	33 ± 6	51 ± 8	247 ± 13	176 ± 13	83 ± 10	58 ± 8
J1633+4718N	205 ± 23	93 ± 19	320 ± 20	96 ± 32	104 ± 32	1023 ± 36	471 ± 36	182 ± 12	142 ± 15
J1633+4718S	203 ± 42	135 ± 16	545 ± 29	167 ± 36	177 ± 67	1163 ± 176	576 ± 76	128 ± 17	114 ± 17
J2258-0115EN	84 ± 12	22 ± 10	96 ± 12	18 ± 9	24 ± 5	273 ± 16	137 ± 15	63 ± 12	43 ± 8
J2258-0115WS	76 ± 39	127 ± 13	425 ± 23	61 ± 8	64 ± 10	128 ± 16	109 ± 11	21 ± 4	20 ± 5
Second phase (10 Dual AGNs)									
J0217-0845EN	44 ± 5	11 ± 3	29 ± 6	55 ± 10	84 ± 9	51 ± 17	69 ± 16	60 ± 12	29 ± 8
J0217-0845WS	47 ± 7	24 ± 4	48 ± 7	62 ± 11	57 ± 11	99 ± 13	124 ± 19	82 ± 17	83 ± 18
J0756+2340EN	150 ± 15	85 ± 16	138 ± 11	51 ± 10	439 ± 65	806 ± 77	656 ± 31	168 ± 13	197 ± 10
J0756+2340WS	80 ± 15	93 ± 16	195 ± 16	66 ± 12	369 ± 37	329 ± 39	397 ± 15	231 ± 29	168 ± 19
J0813+4941WN	92 ± 30	229 ± 29	866 ± 44	105 ± 15	189 ± 47	200 ± 60	278 ± 46	94 ± 27	78 ± 29
J0813+4941ES	171 ± 10	24 ± 10	106 ± 10	40 ± 7	618 ± 135	699 ± 141	332 ± 35	162 ± 27	136 ± 42
J0833+1532WN	30 ± 6	45 ± 10	174 ± 16	25 ± 5	33 ± 13	140 ± 25	222 ± 10	69 ± 12	45 ± 12
J0833+1532ES	206 ± 10	245 ± 18	805 ± 13	51 ± 8	74 ± 34	236 ± 39	127 ± 28	68 ± 9	76 ± 8
J0848+3515EN	277 ± 22	475 ± 23	1408 ± 28	184 ± 16	750 ± 56	1025 ± 88	610 ± 62	156 ± 24	235 ± 19
J0848+3515WS	1773 ± 50	2124 ± 41	6856 ± 70	1549 ± 93	2137 ± 163	2402 ± 120	1529 ± 90	2025 ± 41	1383 ± 42
J0907+5203EN	248 ± 11	165 ± 17	474 ± 18	95 ± 15	361 ± 53	656 ± 51	249 ± 21	181 ± 42	266 ± 29
J0907+5203WS	116 ± 12	209 ± 10	633 ± 10	141 ± 14	109 ± 37	455 ± 31	193 ± 14	180 ± 12	180 ± 17
J1214+2931EN	553 ± 21	930 ± 25	2743 ± 22	287 ± 15	463 ± 16	1239 ± 15	1467 ± 13	598 ± 44	375 ± 35
J1214+2931WS	4452 ± 117	10412 ± 100	31133 ± 105	1489 ± 67	1182 ± 97	9990 ± 145	5413 ± 218	2429 ± 170	2544 ± 204
J1645+2057WN	121 ± 19	77 ± 18	232 ± 13	40 ± 12	123 ± 38	485 ± 63	435 ± 64	95 ± 14	138 ± 16
J1645+2057ES	293 ± 27	76 ± 19	339 ± 16	37 ± 11	327 ± 63	765 ± 56	547 ± 15	137 ± 12	100 ± 10
J2206+0003WN	88 ± 18	49 ± 9	154 ± 17	76 ± 12	144 ± 31	247 ± 27	230 ± 18	163 ± 16	144 ± 15
J2206+0003ES	60 ± 13	67 ± 6	251 ± 12	174 ± 14	335 ± 52	436 ± 79	804 ± 30	437 ± 21	401 ± 17
J2314+0653WN	413 ± 10	608 ± 10	1736 ± 10	216 ± 12	401 ± 27	1087 ± 25	953 ± 20	416 ± 13	371 ± 10
J2314+0653ES	430 ± 19	149 ± 13	376 ± 11	84 ± 17	361 ± 20	1451 ± 25	712 ± 19	339 ± 16	227 ± 14

Notes: Fluxes in units of 10^{-17} erg cm $^{-2}$ s $^{-1}$. The Fluxes of H β and H α emission lines are both for the narrow line component.

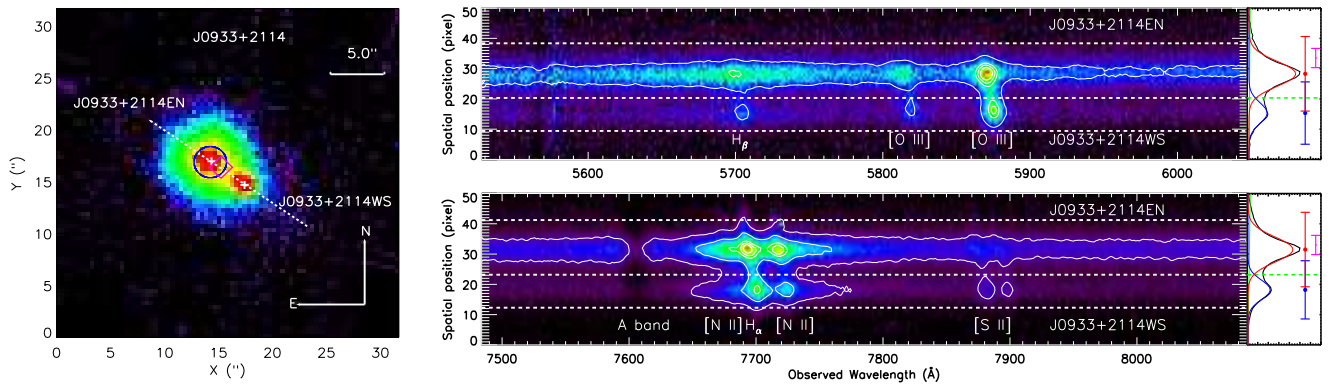


Figure 1. Left: Pseudo color image of J0933+2114 in SDSS g band. The slit of our long-slit observation was positioned to cross the centers of J0933+2114EN and J0933+2114WS, as marked by the white dashed line. The position of the radio source given in the FIRST catalogue is marked by the magenta diamond. The fiber position of the SDSS spectrum is marked by the blue circle. The white pluses indicate positions of the two optical cores. Right: Segments of the two-dimensional long-slit spectrum of J0933+2114. The spectrum exhibits two sets of spatially resolved AGN spectra, corresponding to J0933+2114EN and J0933+2114WS, respectively. The white dashed lines set the boundaries used to extract the 1D spectra of the two cores. More details about extracting 1D spectra are given in Section 2.3.2.

Table 4
BPT classifications

Name	$\log ([\text{O III}]/\text{H}\beta)$	$\log ([\text{N II}]/\text{H}\alpha)$	$\log ([\text{S II}]/\text{H}\alpha)$	$\log ([\text{O I}]/\text{H}\alpha)$	BPT _[NII]	BPT _[SII]	BPT _[OI]	SDSS _C
First phase (6 Dual AGNs)								
J0151–0245WN	0.23 ± 0.02	0.53 ± 0.09	0.59 ± 0.09	0.23 ± 0.08	AGN	LINER	LINER	--
J0151–0245ES	0.30 ± 0.02	0.25 ± 0.03	0.25 ± 0.04	-0.35 ± 0.04	AGN	LINER	LINER	--
J0933+2114EN	BLA	BLA	BLA	BLA	BLA	BLA	BLA	Type I AGN
J0933+2114WS	BLA	BLA	BLA	BLA	BLA	BLA	BLA	--
J1017+3448WN	0.49 ± 0.08	-0.22 ± 0.02	-0.41 ± 0.02	-0.94 ± 0.09	AGN	Seyfert	Seyfert	--
J1017+3448ES	BLA	BLA	BLA	BLA	BLA	BLA	BLA	Type I AGN
J1105+1957EN	-0.00 ± 0.02	-0.14 ± 0.01	-0.38 ± 0.01	-1.33 ± 0.01	Comp	H II	H II	--
J1105+1957WS	0.32 ± 0.06	-0.15 ± 0.01	-0.24 ± 0.01	-0.87 ± 0.04	AGN	Seyfert	Seyfert	Seyfert
J1633+4718N	0.19 ± 0.03	-0.34 ± 0.02	-0.50 ± 0.01	-1.03 ± 0.07	Comp	H II	Seyfert	--
J1633+4718S	BLA	BLA	BLA	BLA	BLA	BLA	BLA	Type I AGN
J2258–0115EN	0.06 ± 0.04	-0.30 ± 0.01	-0.41 ± 0.02	-1.18 ± 0.06	Comp	H II	H II	--
J2258–0115WS	BLA	BLA	BLA	BLA	BLA	BLA	BLA	Type I AGN
Second phase (10 Dual AGNs)								
J0217–0845EN	-0.18 ± 0.04	0.13 ± 0.18	0.24 ± 0.16	0.03 ± 0.15	AGN	LINER	LINER	--
J0217–0845WS	0.01 ± 0.01	0.10 ± 0.07	0.22 ± 0.09	-0.20 ± 0.08	AGN	LINER	LINER	LINER
J0756+2340EN	-0.03 ± 0.04	-0.09 ± 0.05	-0.34 ± 0.05	-1.20 ± 0.06	Comp	H II	H II	--
J0756+2340WS	0.38 ± 0.03	0.08 ± 0.05	0.08 ± 0.06	-0.70 ± 0.07	AGN	LINER	LINER	LINER
J0813+4941WN	BLA	BLA	BLA	BLA	BLA	BLA	BLA	Type I AGN
J0813+4941ES	-0.21 ± 0.03	-0.32 ± 0.05	-0.37 ± 0.06	-1.24 ± 0.06	Comp	H II	H II	--
J0833+1532WN	0.75 ± 0.09	0.20 ± 0.08	-0.09 ± 0.10	-0.73 ± 0.08	AGN	Seyfert	Seyfert	--
J0833+1532ES	BLA	BLA	BLA	BLA	BLA	BLA	BLA	Type I AGN
J0848+3515EN	0.71 ± 0.04	-0.23 ± 0.06	-0.30 ± 0.04	-0.75 ± 0.04	AGN	Seyfert	Seyfert	Seyfert
J0848+3515WS	BLA	BLA	BLA	BLA	BLA	BLA	BLA	Type I AGN
J0907+5203EN	0.28 ± 0.02	-0.42 ± 0.05	-0.17 ± 0.06	-0.84 ± 0.04	Comp	LINER	LINER	Ambiguous AGN
J0907+5203WS	0.73 ± 0.05	-0.37 ± 0.04	-0.10 ± 0.03	-0.51 ± 0.05	AGN	Seyfert	Seyfert	Seyfert
J1214+2931EN	0.69 ± 0.02	0.07 ± 0.01	-0.10 ± 0.03	-0.64 ± 0.01	AGN	Seyfert	Seyfert	Seyfert
J1214+2931WS	BLA	BLA	BLA	BLA	BLA	BLA	BLA	Type I AGN
J1645+2057WN	0.28 ± 0.04	-0.05 ± 0.09	-0.32 ± 0.06	-1.07 ± 0.06	AGN	Seyfert	Seyfert	Seyfert
J1645+2057ES	0.06 ± 0.05	-0.15 ± 0.03	-0.51 ± 0.04	-1.32 ± 0.11	Comp	H II	H II	Comp
J2206+0003WN	0.24 ± 0.05	-0.03 ± 0.06	0.10 ± 0.05	-0.51 ± 0.05	AGN	LINER	LINER	LINER
J2206+0003ES	0.62 ± 0.03	0.27 ± 0.08	0.28 ± 0.08	-0.40 ± 0.09	AGN	LINER	LINER	LINER
J2314+0653WN	0.62 ± 0.01	-0.06 ± 0.01	-0.14 ± 0.01	-0.62 ± 0.03	AGN	Seyfert	Seyfert	Seyfert
J2314+0653ES	-0.06 ± 0.02	-0.31 ± 0.01	-0.41 ± 0.01	-1.23 ± 0.04	Comp	H II	H II	--

Notes: BPT_[N II], BPT_[S II], BPT_[O I]: Result of BPT classifications in the $\log ([\text{O III}]/\text{H}\beta) - \log ([\text{N II}]/\text{H}\alpha)$, $\log ([\text{O III}]/\text{H}\beta) - \log ([\text{S II}]/\text{H}\alpha)$ and $\log ([\text{O III}]/\text{H}\beta) - \log ([\text{O I}]/\text{H}\alpha)$ planes, respectively. Seyfert: Seyfert galaxy. BLA: Broad line AGN (Type I AGN). Comp: AGN/Star-forming composite galaxy. H II: Star-forming region. LINER: Low ionization nuclear emission line region. Ambiguous AGN: Galaxy of ambiguous classification, i.e. those classified as one type of AGN in one or two of the BPT diagram(s) but as another type of AGN in other remaining diagram(s). SDSS_C: Classification based on BPT diagrams redrawn with the SDSS data.

per pixel on the sky, covering a field of view of about 9.6×9.6 square arcmin.

Several grisms of different spectral resolutions and wavelength range are available for YFOSC. The spectrograph can be used in long-slit mode with several slits of different widths available. We note the overall sensitivity of the grisms⁸ (including telescope and detectors) are about 10 to 20 per cent and even > 5 per cent at the blue beginning and red end. For each candidate, the two optical cores are spatially resolved in the SDSS images and the slit is set to pass through the two cores of the merging galaxies. For this purpose, the spectrograph is rotated with a specific position angle (PA) for each galaxy pair and the values of PA for the individual systems are presented in Table 2. In this way, we obtain 2D spatially resolved spectra for the two cores in the merging systems, under good seeing condition.

The ASTRO-DARING project was started in 2014 November. All observations presented here were carried out with the YFOSC in long-slit mode using several slits of fixed widths, depending on the observing condition, especially the seeing and transparency. Depending on the grisms used, our observations can be divided into two phases. The first phase is

from November 2014 to November 2015. During this period, we mainly use two grisms: a blue one G14 covering 3600 to 7500 Å and a red one G8 covering 5100 to 9600 Å. A slit of width 1.8'' matching the typical seeing was used during this phase. With the above combinations, the typical resolution are about $330 \pm 20 \text{ km s}^{-1}$, $500 \pm 40 \text{ km s}^{-1}$ for G8, G14 Grisms respectively (Table 1). In total, 15 targets were observed during this period.

Due to the increasing seeing and decreasing transparency (possibly caused by the El Niño effects⁹), we changed to use G3 that has a higher efficiency than G14 and G8 but a lower resolution in the second phase (from November 2015 to February 2017). The spectra obtained cover the whole optical wavelength range (3400 to 9100 Å)¹⁰. Depending on the seeing condition, a slit of width 1.8'' or 2.5'' was adopted. The resulting spectral resolution was relatively low with FWHMs of $730 \pm 60 \text{ km s}^{-1}$, $970 \pm 70 \text{ km s}^{-1}$, respectively, for the

⁹ El Niño effects results from the rise of sea surface temperatures in the Indian Ocean. It may not bring drought but cause heavy rainfall at certain periods.

¹⁰ We note that the effect of the second-order contamination at the wavelength smaller than 4550 Å is largely smaller than 5-10 per cent. Moreover, the current analysis is not affected by this issue since all of our concerned emission lines are longer than 4550 Å.

⁸ The wavelength of the adopted grisms are present in Table 1.

1.8", 2.5" slits of G3 Grism. In this phase, a total of 26 targets were observed.

Totally, we obtained long-slit spectra for 41 candidates between November 2014 and February 2017 using the YFOSC. For more details, see the observational log in Table 2.

2.3. Data Reduction

2.3.1. Wavelength & Flux calibration

The data were reduced with IRAF¹¹ and IDL routines. The 2D spectra were bias subtracted, flat-fielded calibrated, cosmic-rays fully removed (using the IRAF task `crmedian`), wavelength calibrated, and flux calibrated on 2D with IRAF. The wavelength and flux calibrations were applied to all 2D spectra. The wavelength distortions in the spatial direction were carefully corrected using 2D wavelength map constructed by arc frame performed on IRAF. The ESO spectroscopic standard stars observed in the same night was applied to the flux calibrations. The sky background is subtracted in 2D manner by the `background` implemented in IRAF. The above steps were all carried out with IRAF for the 2D spectra. After those, the IDL routine is adopted to extract the final 1D spectra. More details about this step are presented below.

2.3.2. Extraction of 1D spectra

To explore the activity natures of the two cores in the merging system, 1D spectra of the two cores in the system are extracted from the spatially resolved 2D spectrum. When extracting the 1D spectra, flux loss and contamination are unavoidable as the spectra of the two cores are close to each other. We therefore developed a 1D extraction method by achieving a tradeoff between reducing flux loss and contamination.

An example of the 1D extraction is shown in Fig. 1. The flux distribution along the spatial direction is contributed by the two galaxies/AGNs and the sky background residuals. We assumed that the contribution from each of the two nuclei can be represented by a Gaussian, while that of the residual sky background can be represented by a first-order polynomial accounting for any systematic pattern left in the subtracted background. To extract the spectrum of each galaxy/AGN, the flux distribution is fit by two Gaussians plus a first-order polynomial and the 1D spectra of each two galaxy/AGN are obtained as shown in the right panel of Fig. 1. The inner/outer boundaries in Fig. 1 is set when the 1D spectra of two cores are extracted from the 2D spectrum. The outer boundary of each of the two galaxies/AGNs is defined as the position of two-sigma width from the center of the fitted Gaussian. This was chosen in order to enclose as much of the flux from the target but as possible with minimum noise from the background (see the two white dashed lines on the two-sides of the galaxies/AGNs in the right panel of Fig. 1). For the central overlapping region of the two galaxies/AGNs, the position of equal flux of the two fitted Gaussians is selected as the inner boundary to minimize the flux loss and contamination of each target (see the middle white dashed line in the right panel of Fig. 1). Given the above extraction procedures, the true flux of one target is assumed by the total flux under the fitted Gaussian and then the flux loss is given by the total area beyond the inner and outer boundaries of the fitted Gaussian. The flux contamination is defined as the total flux tail between the extracted inner and

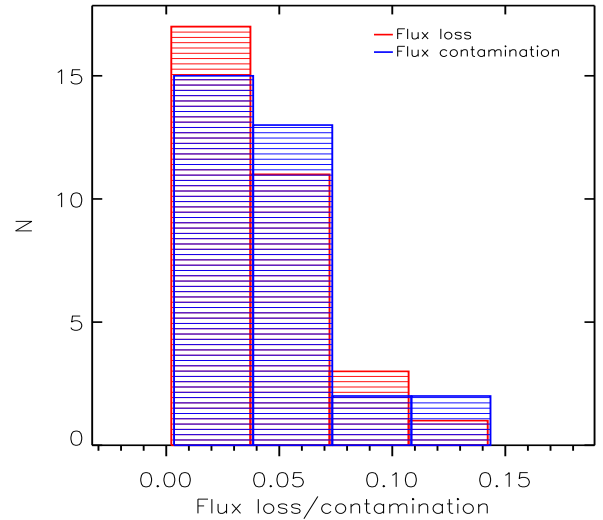


Figure 2. Distribution ratios of flux loss and contamination of the extracted 1D spectra. The flux loss ratio is given by the ratio between the flux loss and the true flux of specified target and the flux contamination ratio is defined as the flux contamination to the actual extracted flux between the inner and outer boundaries of specified target (see Fig. 1).

outer boundaries, extended from the nearby target (true flux also represented by another fitted Gaussian). We note that the extraction limits (the inner/outer boundaries) are for purposes of summing across the spatial dimension.

To account for the effects of possible slit tilt, the whole long-slit spectrum is divided into six slices¹² along the wavelength direction and the 1D spectra in each slice are extracted with the above procedure. Given the relatively large angular separations of our selected candidates, the spectra of the two cores in merging galaxies are well separated in general and their 1D spectra can be extracted with minimum flux loss and contamination. To quantitatively show the robustness of our 1D spectral extraction procedure, we calculate the averaged flux loss and contamination ratios of the six slices for our observed targets. The distributions of flux loss and contamination of the 1D spectra of our dual AGN candidates are shown in Fig. 2. In general, the flux loss and contamination amount to only a few per cent. This is corroborated by the high-quality example spectra presented in Fig. 3. Part of our targets have multiple observations and their 1D spectra are stacked via their signal-to-noise ratios (SNRs).

2.3.3. Subtraction of contribution of host galaxy

The continuum and absorption features of host galaxy should be subtracted properly from the extracted spectra before deriving the properties of emission lines. To subtract the continuum and absorption features, the penalised PiXel Fitting software (pPXF, Cappellari & Emsellem 2004, Cappellari 2017) was applied to our long-slit spectra. This code allows one to fully decompose gas emission from stellar absorption features, using a maximum penalized likelihood approach. In pPXF, the MILES library¹³

¹² The tilt angle of YFOSC slits are largely adjusted to 0.3-0.5 degrees and thus the tilt changes are within 1-3 pixels along the whole slices (each with a length about 300 pixels). In addition, six slices are enough to account for the point spread function (PSF) along the wavelength direction (mostly within 1-2 pixels).

¹³ This library contains 985 flux well-calibrated stellar spectra with wavelength range from 3525 Å to 7500 Å, with a spectral resolution of FWHM ~

¹¹ <http://ast.noao.edu/data/software>

(Sánchez-Blázquez et al. 2006) with wide ranges of physical parameters was adopted as template to model the contribution from host galaxy. Before fitting, all the template spectra were properly convolved to the resolution of our long-slit spectra and all the prominent emission lines were masked. As an example, the performance of this subtraction was shown in Fig. 3 for J0933+2114 system (as well as in the Appendix B for more examples). The consistent results of flux ratio and FWHM measurements from LJT long-slit spectra and SDSS fiber spectra as checked in Section 3.3 show that the host subtraction by pPXF algorithm is generally reasonable for our low-resolution LJT spectra.

2.3.4. Detections of emission lines

Typically, 9 strong optical emission lines (i.e., $H\beta$, [O III] $\lambda\lambda 4959, 5007$, [O I] $\lambda 6300$, $H\alpha$, [N II] $\lambda\lambda 6549, 6583$, [S II] $\lambda\lambda 6717, 6731$) can be detected from the spectra with continuum and absorption features properly subtracted by pPXF described in above section. Line properties (e.g., flux, FWHM, central wavelength) can be derived by an IDL fitting procedure MPFIT¹⁴ (Craig Markwardt 2009). We fit each component of detected emission lines by single or multiple Gaussian(s) to obtain their fluxes, central wavelengths and FWHMs¹⁵. Here we note that a emission line could be detected only with signal-to-noise ratio (SNR; defined as the ratio between the peak of emission line and the standard deviation of the continuum nearby the emission line) greater than 3. For the case shown in Fig. 4, we use one Gaussian for the [N II] $\lambda 6550$ line, one Gaussian for the [N II] $\lambda 6585$ line and a pair of Gaussians with the same central wavelength for the broad and narrow $H\alpha$ components. If only a narrow component of the $H\alpha$ emission detected, then only one Gaussian is used to fit it. Similar fitting strategy is used for other detected emission lines. The error of each parameter is given by the covariance matrix provided by MPFIT. The fitting results of all well detected emission lines are presented in Table 3 and Table A1.

3. RESULTS

3.1. Identification and classification of AGNs

In this Section, we attempt to identify AGNs and classify them from the observed targets based on the analysis of the measured emission lines in the optical range. The details are given in the following. We also indicate the caveats of the current AGN identifications purely based on optical data at the end of this Section.

Here, we adopt the criteria developed by Hao et al. 2005 to identify Type I AGN: 1) FWHM of $H\alpha > 1200 \text{ km s}^{-1}$ and $h(H\alpha \text{ broad})/h(H\alpha \text{ narrow}) > 0.1$; or 2) FWHM of $H\alpha > 2200 \text{ km s}^{-1}$, where $h(H\alpha \text{ broad})$ and $h(H\alpha \text{ narrow})$ are the heights of $H\alpha$ broad and narrow line components, respectively. The height is given by the peak of the Gaussian fits.

For Type II AGN (i.e., those with narrow emission lines), we adopt the so-called BPT diagrams (see Baldwin et al. 1981, Veilleux & Osterbrock 1987, Kewley et al. 2001, hereafter Ke01, Kauffmann et al. 2003, hereafter Ka03, Kewley et al. 2006, hereafter Ke06) to identify them, based on the four optical emission line flux ratios, i.e., [O III]

$\lambda 5007/H\beta$, [N II] $\lambda 6583/H\alpha$, [S II] $\lambda\lambda 6717, 6731/H\alpha$, and [O I] $\lambda 6300/H\alpha$. The fluxes used have not been corrected for any reddening and extinction effects. As the lines involved in those ratios have close central wavelengths, the non-consideration of reddening corrections has minor impact on the results (e.g., Kauffmann et al. 2003). The so-called “maximum starburst line” on the the BPT diagram is derived from the upper limit of the theoretical pure stellar photoionization models (Ke01, Ka03, Ke06). As Fig. 5 shows, sources above the red solid line (Ke01) are likely to be dominated by AGNs, below the blue dashed line (Ka03) are purely star-forming galaxies, between the red solid line (Ke01) and the blue dashed line (Ka03) are AGNs/star-forming composite galaxies (Comp). In the AGN region, Seyferts and LINERs populate dominantly above and below the blue solid line (Ke06), respectively. More details of the BPT diagrams are described in Kewley et al. (2006). Based on those BPT diagrams, the galaxies are classified into star-forming galaxies (H II), AGN/star-forming composite galaxies (Comp), Seyfert galaxies (Seyfert), low ionization nuclear emission line region (LINER) and ambiguous galaxies (ambiguous AGN). Ambiguous galaxies are those that classified as one subtype of AGN in one or two of the diagram(s) but classified as another subtype of AGN in the remaining diagram(s). The detail classifications of our dual AGNs is presented in Table 4.

The BPT diagrams have been widely used to identify optical AGNs. However, some caveats remain when using the BPT diagrams. We note that the LINERs, Comps and ambiguous galaxies identified by the BPT technique may suffer contamination from the H II or star-forming galaxies, given the current line ratio measurements errors and the potential systematics of the theoretical criteria (e.g., Kauffmann & Heckman 2009; Stern & Laor 2013; Azadi et al. 2017). Some studies also indicate that the distinct regions of AGN and H II on the BPT diagrams have some overlaps (e.g., Kauffmann & Heckman 2009; Heckman & Best 2014). This empirical identification will miss the lineless AGNs, due to their extremely weak, sometimes completely undetected emission lines (Cid Fernandes et al. 2010; Netzer 2015). Not all of the AGN populations can be recovered by only using a single waveband observation (e.g., Azadi et al. 2017). The further follow-up observations by either radio or X-ray could provide more vital constraints on the nature of the identified dual AGNs. It is worth mentioning that identifying outflows in these optical emission line profiles could further provide indirect evidence on the nature of our dual AGN candidates, since the outflows around NLR can be driven by AGN feedback (e.g., Di Matteo et al. 2005; Hopkins et al. 2005; Crenshaw et al. 2015; Müller-Sánchez et al. 2016; Nevin et al. 2018). However, as shown in Nevin et al. (2018), the velocity offset of the outflows are typically within 1000 km s^{-1} , and the current spectroscopy observations ($R \sim 300$) can not be used to identify such outflow features. Our ongoing long-slit spectroscopy observations by the Double Spectrograph (DBSP) with resolving power around 2000 mounted on Hale 5.1m telescope will allow us to do such analysis and provide more constraints on the nature of the dual AGN candidates.

3.2. Dual AGN sample

Based on long-slit observations of 41 candidates with the YFOSC and the identification criteria presented in Section 3.1, we have found 16 likely dual AGNs. For the remaining 25 targets, 12 of them are AGN and normal galaxy pairs,

2.51 Å, $\sigma \sim 64 \text{ km s}^{-1}$.

¹⁴ <https://pages.physics.wisc.edu/craigm/idl/fitting.html>

¹⁵ The FWHM values reported in Table 5 have been corrected for the instrumental broadening effect.

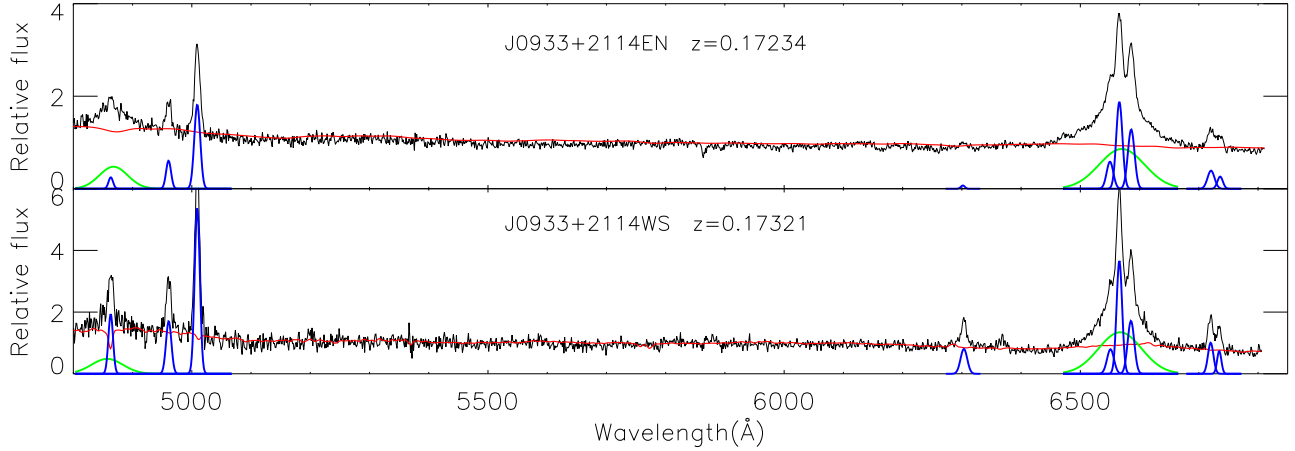


Figure 3. The LJT spectra of dual AGN: J0933+2114 respectively for J0933+2114EN (top) and J0933+2114WS (bottom) showing emission lines H β , [O III] $\lambda\lambda$ 4959,5007, [O I] λ 6300, H α , [N II] $\lambda\lambda$ 6549,6583 and [S II] $\lambda\lambda$ 6717,6731 at rest-frame wavelengths. We used pPXF to subtract continuous spectrum and got emission lines. The red lines represent the continuum component of host galaxy, the blue lines represent the narrow emission lines component and the green lines represent the broad emission lines component.

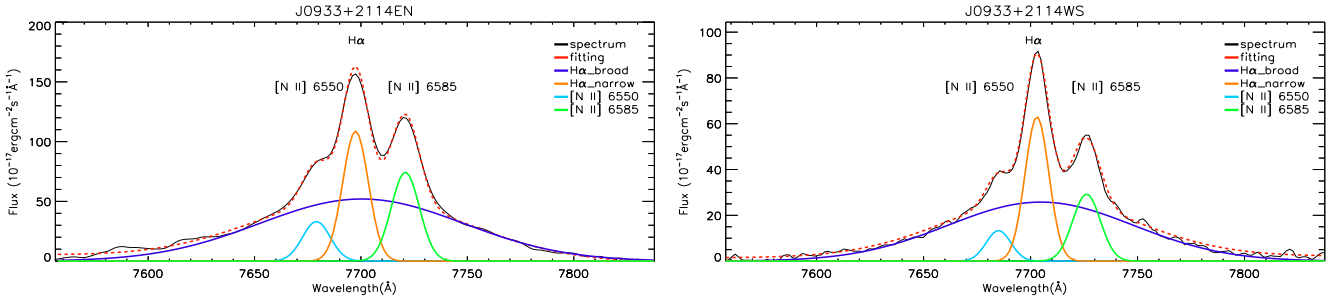


Figure 4. Spectra fitting for J0933+2114EN (left) and J0933+2114WS (right) near the H α region. Both galaxies have a broad H α component. We use one Gaussian for [N II] λ 6549, another Gaussian for [N II] λ 6583 and a pair of Gaussians for the H α broad and narrow components that have the same central wavelength, to fit the whole spectral region.

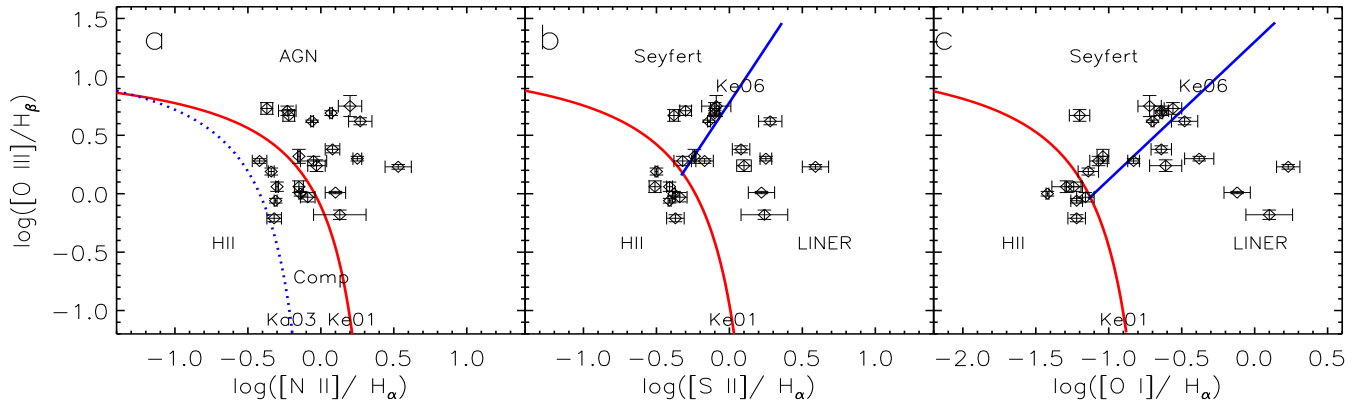


Figure 5. BPT diagrams of our dual AGNs. Detailed information about the classifications of the individual galaxies is shown in Table 4.

5 of them are AGN and star-forming galaxy pairs, 1 target is an AGN and star nonphysical pair and other 7 targets are hard to identify either due to the unresolved 2D long-slit spectra or low quality spectra. In our dual AGN sample, 15 are newly found and only one (J1214+2931) has been revealed with X-ray image by Secrest et al. (2017). The detailed properties of the 16 likely dual AGNs are presented in Table 5. The high efficiency of our systematic searching method is about 39 per cent (16/41). Amongst our identified dual AGNs, 28.1 per cent (9/32) are Type I AGNs, 25.0 per cent (8/32) Seyfert 2,

21.9 per cent (7/32) LINERs, 18.8 per cent (6/32) Comp and 6.3 per cent (2/32) ambiguous classification.

As an example, we briefly discuss the properties of dual AGN J0933+2114. As shown in Fig. 1, the two spectra of the dual cores, i.e. J0933+2114EN and J0933+2114WS, are spatially well resolved, allowing robust identification and classification of the system.

J0933+2114EN has the redshift of 0.17234 ± 0.00005 and the FWHM of the NLR is $629 \pm 46 \text{ km s}^{-1}$ as measured from the [O III] λ 5007 line. The spectrum of J0933+2114EN has

Table 5
Dual AGNs

Name	AGN	Z_m	FWHM_{NLR} (km s^{-1})	FWHM_{BLR} (km s^{-1})	V_{offset} (km s^{-1})	Sep ($''/\text{kpc}$)	$W_1 - W_2$ mag	Radio	Classification
First phase (6 Dual AGNs)									
J015107.39-024526.87	J0151-0245WN	0.04774 ± 0.00008	262 ± 63	---	57 ± 28	5.1/4.8	0.030	N	LINER
	J0151-0245ES	0.04793 ± 0.00005	471 ± 36	---	---	---	---	Y	LINER
J093347.76+211436.41	J0933+2114EN	0.17234 ± 0.00005	629 ± 46	5091 ± 153	261 ± 21	4.2/12.3	0.714	Y	Type I AGN
	J0933+2114WS	0.17321 ± 0.00005	548 ± 53	4956 ± 155	---	---	0.873	N	Type I AGN
J101757.07+344846.61	J1017+3448WN	0.14321 ± 0.00005	778 ± 41	---	243 ± 21	5.6/14.2	0.993	Y	Seyfert
	J1017+3448ES	0.14402 ± 0.00005	614 ± 48	3255 ± 243	---	---	0.872	N	Type I AGN
J110544.48+195750.06	J1105+1957EN	0.10421 ± 0.00005	487 ± 46	---	84 ± 21	3.9/7.4	0.329	Y	Comp
	J1105+1957WS	0.10449 ± 0.00005	399 ± 50	---	---	---	---	N	Seyfert
J163323.58+471858.95	J1633+4718N	0.11525 ± 0.00005	413 ± 71	---	153 ± 21	3.8/8.0	0.812	N	Ambiguous AGN
	J1633+4718S	0.11576 ± 0.00005	517 ± 57	1989 ± 248	---	---	---	Y	Type I AGN
J225810.01-011516.26	J2258-0115EN	0.11609 ± 0.00005	738 ± 43	---	300 ± 21	3.2/6.9	0.652	Y	Comp
	J2258-0115WS	0.11709 ± 0.00005	650 ± 46	2929 ± 347	---	---	---	N	Type I AGN
Second phase (10 Dual AGNs)									
J021703.81-084515.97	J0217-0845EN	0.1078 ± 0.0001	339 ± 237	---	90 ± 40	6.0/12.0	0.191	N	LINER
	J0217-0845WS	0.1081 ± 0.0001	670 ± 164	---	---	---	0.202	Y	LINER
J075621.37+234043.97	J0756+2340EN	0.0745 ± 0.0001	806 ± 151	---	120 ± 40	6.8/9.6	0.255	Y	Comp
	J0756+2340WS	0.0741 ± 0.0001	565 ± 195	---	---	---	---	N	LINER
J081347.49+494109.83	J0813+4941WN	0.0942 ± 0.0001	804 ± 138	2640 ± 123	150 ± 40	3.3/5.8	0.935	Y	Type I AGN
	J0813+4941ES	0.0947 ± 0.0001	521 ± 212	---	---	---	---	N	Comp
J083355.49+153236.62	J0833+1532WN	0.1514 ± 0.0001	427 ± 285	---	60 ± 40	4.5/11.9	0.768	Y	Seyfert
	J0833+1532ES	0.1516 ± 0.0001	486 ± 227	3322 ± 167	---	---	---	N	Type I AGN
J084809.69+351532.12	J0848+3515EN	0.0573 ± 0.0001	496 ± 272	---	60 ± 40	5.6/6.2	0.632	N	Seyfert
	J0848+3515WS	0.0571 ± 0.0001	498 ± 221	2494 ± 126	---	---	---	Y	Type I AGN
J090714.61+520350.61	J0907+5203EN	0.0601 ± 0.0001	815 ± 102	---	150 ± 40	7.4/8.5	0.429	Y	Ambiguous AGN
	J0907+5203WS	0.0596 ± 0.0001	709 ± 117	---	---	---	0.368	N	Seyfert
J121418.25+293146.70	J1214+2931EN	0.0633 ± 0.0001	576 ± 191	---	60 ± 40	7.9/9.3	0.059	N	Seyfert
	J1214+2931WS	0.0635 ± 0.0001	648 ± 170	2417 ± 117	---	---	1.274	Y	Type I AGN
J164507.91+205759.43	J1645+2057WN	0.1301 ± 0.0001	644 ± 85	---	270 ± 40	4.2/9.8	0.569	N	Seyfert
	J1645+2057ES	0.1310 ± 0.0001	833 ± 64	---	---	---	---	Y	Comp
J220634.97+000327.57	J2206+0003WN	0.0466 ± 0.0001	889 ± 157	---	120 ± 40	4.7/4.3	0.107	N	LINER
	J2206+0003ES	0.0462 ± 0.0001	650 ± 185	---	---	---	---	Y	LINER
J231439.21+065312.97	J2314+0653WN	0.0876 ± 0.0001	393 ± 141	---	90 ± 40	4.1/6.7	0.679	Y	Seyfert
	J2314+0653ES	0.0879 ± 0.0001	419 ± 133	---	---	---	0.280	N	Comp

Notes: Z_m : Median redshift of main emission lines detected with good SNRs. FWHM_{NLR} : FWHM of narrow line region represented by the FWHM of [O III] $\lambda 5007$ line. FWHM_{BLR} : FWHM of broad line region represented by the FWHM of $\text{H}\alpha$ broad component. V_{offset} : Velocity offset of the two AGN cores. Sep: Separation of the two AGN optical cores in arcsec and in kpc. $W_1 - W_2$: Magnitude difference in WISE W_1 and W_2 bands for the two resolved/unresolved cores. Radio: N (NO), Y (YES), whether detected as the radio-excess AGN result from radio power versus $\text{H}\alpha$ luminosity. SyII: Seyfert 2. Classification: Classifications of the two AGN optical cores.

a broad line component as shown in Fig. 4. The FWHM of the BLR is $5091 \pm 153 \text{ km s}^{-1}$ as given by the $\text{H}\alpha$ broad line component. This value of BLR is much greater than 2200 km s^{-1} , thus J0933+2114EN is clearly a Type I AGN.

J0933+2114WS has a redshift of 0.17321 ± 0.00005 and the FWHM of the NLR is $548 \pm 53 \text{ km s}^{-1}$, again measured from the [O III] $\lambda 5007$ line. J0933+2114WS also has a broad line component as shown in Fig. 4. The FWHM of the the BLR is $4956 \pm 155 \text{ km s}^{-1}$ as measured from the $\text{H}\alpha$ broad line component. The velocity of the BLR is again greater than 2200 km s^{-1} , confirming it a Type I AGN.

J0933+2114 is thus identified as a dual AGN composed of two Type I AGNs. The two optical cores have a separation of 12.3 kpc and a velocity offset of $261 \pm 21 \text{ km s}^{-1}$.

The distribution of dual AGNs identified in the current work in the plane of redshift versus projection distance is presented in Fig. 6, together with those previously known in the literature (Paper I). Dual AGNs detected with hard X-ray or radio observations have redshifts systematically smaller than those found by the double peak technique. Dual AGNs identified in the current work have redshifts ranging from 0.0461 to 0.1722 and separations ranging from 4.3 kpc to 14.2 kpc. As Fig. 6 shows, our dual AGN found in this work make the dual AGN sample more complete in redshift space. For our sample, the

velocity offsets of the two cores range from 57 km s^{-1} to 300 km s^{-1} (Fig. 7), in good agreement with previous results ($50\text{--}300 \text{ km s}^{-1}$; Comerford et al. 2013; Koss et al. 2016).

Detailed analyses of the remaining 15 likely dual AGNs in the current work are presented in Appendix A. In total, we have found 16 likely dual AGNs and significantly increased the number of known dual AGNs.

3.3. Validation of measurements

Given the relatively low resolution of our spectra (especially those of G3), the accuracies of flux ratio, redshift, separation and FWHM measurements presented here should be examined. Doing so, we compare our results with those derived from the SDSS fiber spectra that have a higher spectral resolution ($R \sim 2200$).

3.3.1. Flux ratios

To check the reliability of our BPT diagram results, the flux ratios of our likely dual AGNs are compared to those derived from the SDSS spectra for part of optical cores. First, we compare the flux ratios measured from our long-slit spectra with those from the SDSS fiber spectra. For most of the two cores in dual AGNs, only one core has been identified as AGN in SDSS and another core has no SDSS spectrum. There are

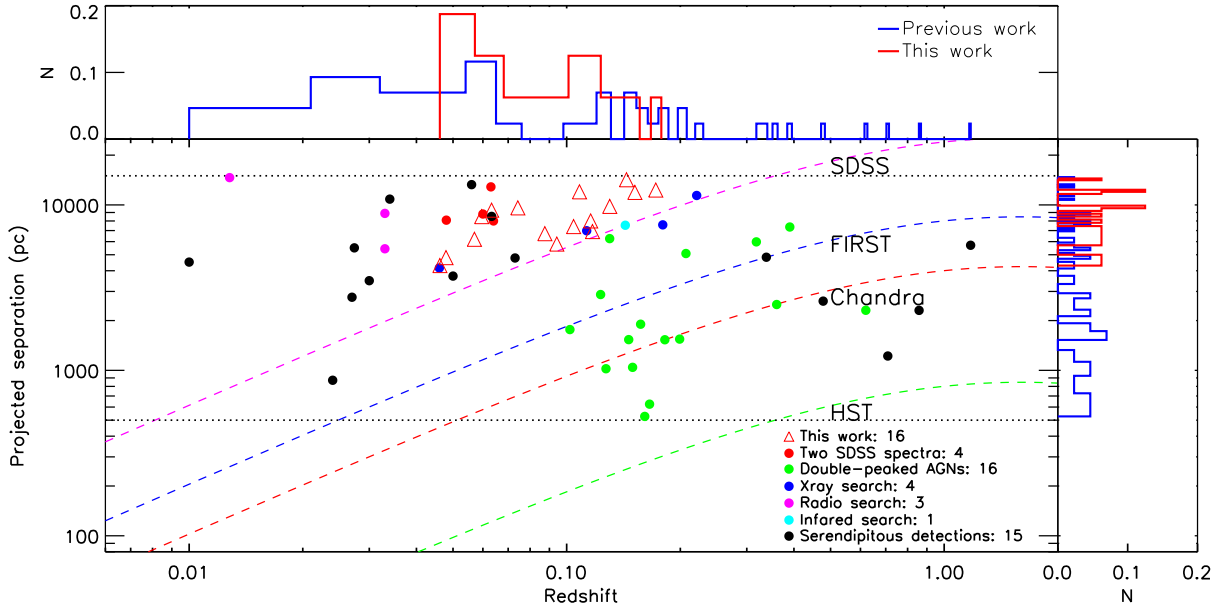


Figure 6. Dual AGNs from the current and previous work. The magenta, blue, red, green dashed lines, respectively, represent the critical resolutions of SDSS spectroscopy, FIRST, Chandra, HST catalogs, i.e., $3.0''$, $1.0''$, $0.5''$, $0.1''$, respectively. The two horizontal dashed lines are the typical separations, i.e., 0.5 and 15 kpc, of dual AGNs, respectively. The top sub-panel shows the number distribution along the redshift for the dual AGNs found previously (blue line) and in this work (red line), respectively. A gap of the distribution of the dual AGNs from previous work now is filled by our sample significantly. The right sub-panel shows the number distribution along the projected separation for the dual AGNs found previously (blue line) and in this work (red line), respectively.

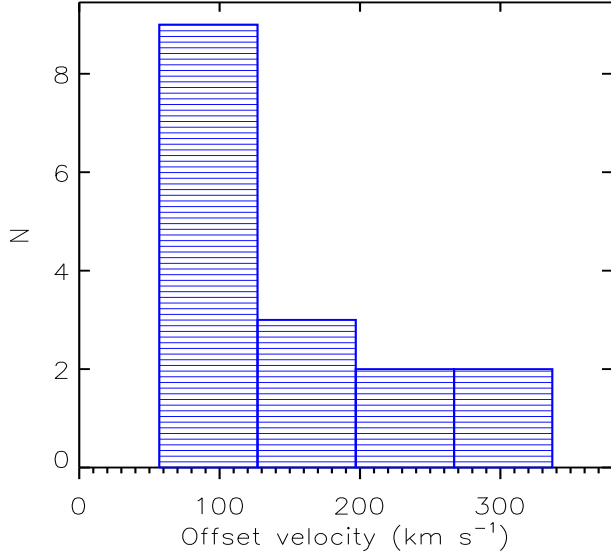


Figure 7. Velocity offsets of the two cores for our dual AGN sample.

32 optical cores in 16 dual AGNs, but only 20 cores have SDSS spectra (Table 4). As Fig. 8 shows, flux ratio measurements from our spectra are generally consistent with those from the SDSS. Here we note that the flux measurements of emission lines from SDSS spectra are similar to those of our long-slit spectra as described in Sections 2.3.3 and 2.3.4. As shown in Table 4, BPT classifications based on the flux ratio measurements from our long-slit spectra are totally in agreement with those based on the SDSS spectra, implying the reliability of the former measurements.

3.3.2. Redshifts

To check the wavelength calibration accuracy of our long-slit spectra, the derived redshifts of those likely dual AGNs are compared to those deduced from the SDSS spectra. The distribution of redshifts of the targeted candidates and our dual AGNs is displayed in Fig. 9. As shown in Fig. 10, the results agree with each other very well. The median value and standard deviation of the redshift differences are only 10 and 23 km s^{-1} , respectively, confirming the good wavelength calibration of our long-slit spectra.

3.3.3. Separations

To check whether the 2D spectra are actually from the two optical cores of our selected merging galaxies, the separations between the two cores from SDSS images are compared to those from the 2D spectra for the 16 identified dual AGNs. Fig. 11 clearly shows the separations fitted from the 2D spectra are in excellent agreement with those from SDSS images. The median value and standard deviation of the separation differences are just 0 and 0.2 kpc, respectively, confirming that our observed 2D spectra are actually from the two cores of merging galaxies.

3.3.4. FWHMs

FWHM is an important parameter that characterizes the NLR and BLR of an AGN. The velocity width of BLR is large enough to be resolved by our spectra and is thus well measured. For the NLRs, the instrumental broadening of our spectra is comparable or slightly higher than their velocity widths. By comparing with the FWHMs deduced from the SDSS spectra, we examine the accuracy of the FWHMs of NLRs measured from our spectra. The results plotted in Fig. 12 show reasonable agreement. The median value and standard deviation of the differences are only 7 and 120 km s^{-1} , respectively.

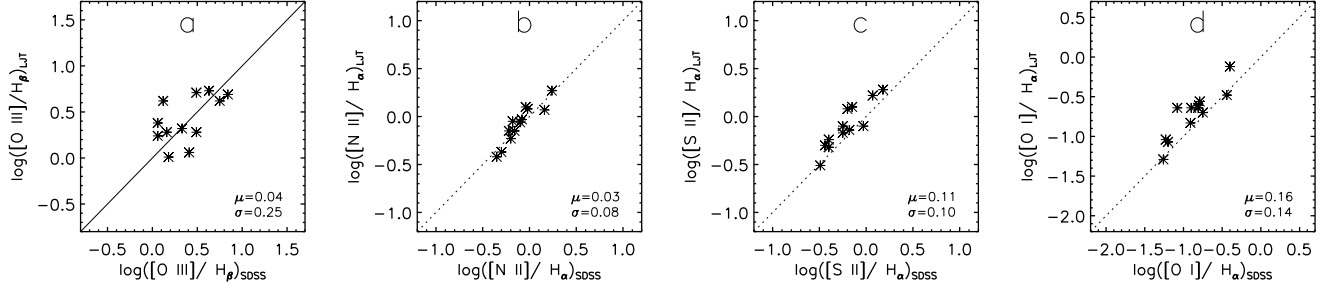


Figure 8. Comparisons of flux ratios as measured from our long-slit and SDSS fiber spectra, for, from left to right, a: $\log([\text{O III}]/\text{H}\beta)_{\text{LJT}}$ v.s. $\log([\text{O III}]/\text{H}\beta)_{\text{SDSS}}$. b: $\log([\text{N II}]/\text{H}\alpha)_{\text{LJT}}$ v.s. $\log([\text{N II}]/\text{H}\alpha)_{\text{SDSS}}$. c: $\log([\text{S II}]/\text{H}\alpha)_{\text{LJT}}$ v.s. $\log([\text{S II}]/\text{H}\alpha)_{\text{SDSS}}$. d: $\log([\text{O I}]/\text{H}\alpha)_{\text{LJT}}$ v.s. $\log([\text{O I}]/\text{H}\alpha)_{\text{SDSS}}$.

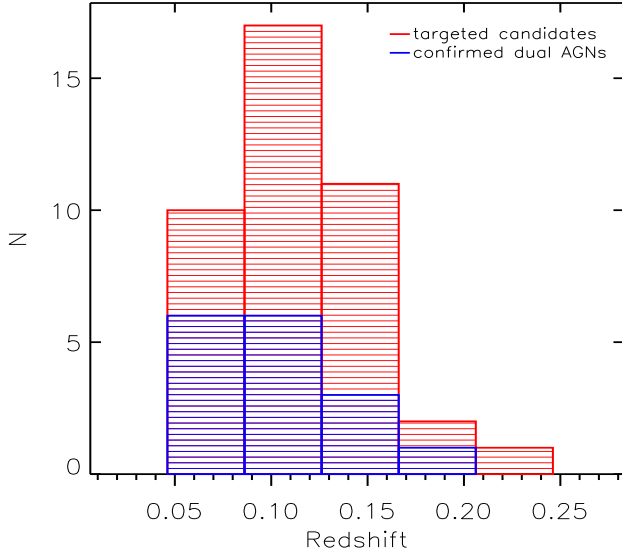


Figure 9. Redshift distribution for our targeted (red) and dual AGNs (blue).

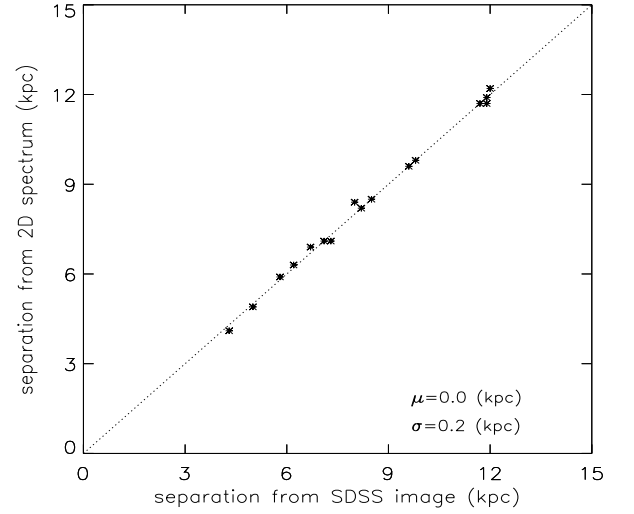


Figure 11. Comparison of separations measured from 2D spectra and from SDSS images for the 16 identified dual AGNs.

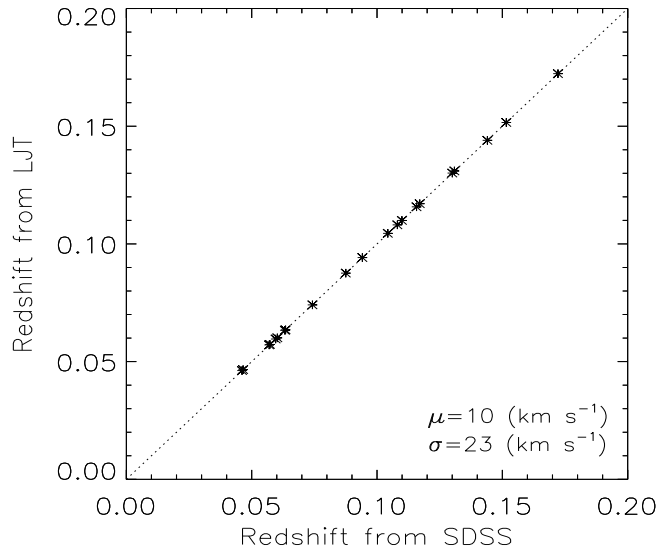


Figure 10. Comparison of redshifts yielded by our long-slit and SDSS spectra for part of cores in our dual AGN sample.

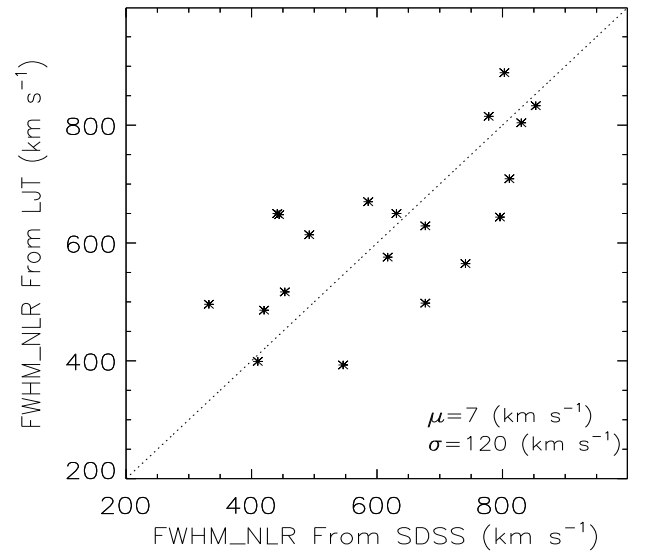


Figure 12. Comparison of FWHMs of NLRs measured from our long-slit and SDSS spectra for part of cores in our dual AGN sample.

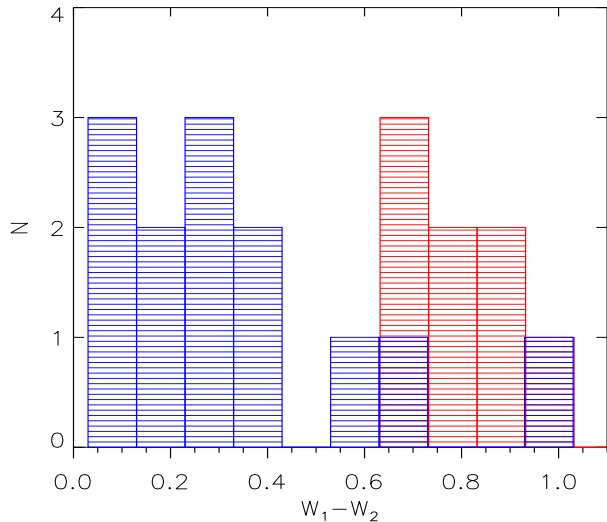


Figure 13. Distribution of $W_1 - W_2$ colors of dual AGNs. The red shaded columns represent Type I AGNs or dual AGNs that contain at least one Type I AGN, while the blue columns represent Type II AGNs or dual AGNs that contain only Type II AGN.

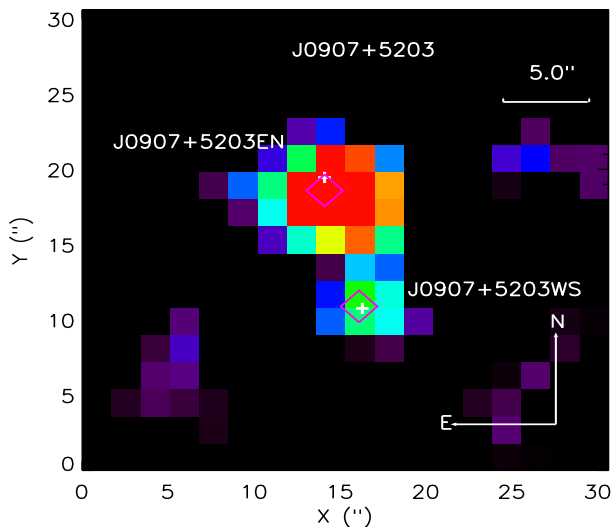


Figure 14. Two radio detections of dual AGN: J0907+5203 from the FIRST catalogue. The positions of the two radio detections are marked by magenta diamonds. The white pluses indicate the positions of the two optical cores.

4. DISCUSSION

4.1. Implications for dual AGN systematic searching

A systematic search for dual AGNs generally includes three steps. To start with, a large sample of potential candidates of dual AGNs is required. Then, follow-up spectroscopy is carried out to exclude most contamination. As a final step, radio or hard X-ray observations provide vital evidence of activity. In this process, the first step is the key to obtaining a large sample of candidate dual AGNs. As mentioned in Section 1, several previous attempts proposed to systematically search for dual AGNs, including that based on DPAGNs (e.g., Liu et al. 2010a; Liu et al. 2011; Shen et al. 2011; Comerford et al. 2012) and the infrared colors of AGNs (e.g., Satyapal et al. 2014, 2017).

Hundreds of DPAGNs have been selected from the DEEP2 Galaxy Redshift Survey (e.g., Gerke et al. 2007) and from

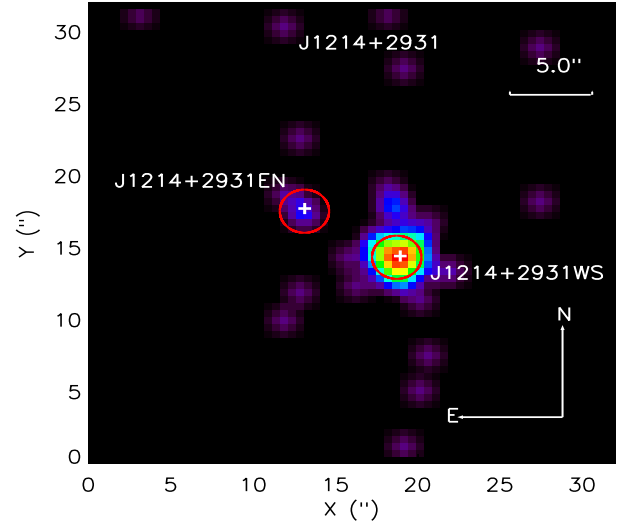


Figure 15. Double X-ray cores of dual AGN: J1214+2931 from the Chandra catalog. In this image, the positions of the two X-ray cores from the Chandra observation are marked by the red circles. The white pluses indicate the positions of the two optical cores.

the SDSS survey (e.g., Wang et al. 2009; Liu et al. 2010a; Smith et al. 2010). However, follow-up spectroscopic observations reveal that only 2 to 5 per cent of the selected DPAGNs are bona fide dual AGNs (e.g., Liu et al. 2011; Shen et al. 2011; Comerford et al. 2012). The main reason underlying this low efficiency is the large contamination of rotating disks or bi-conical outflows of the NLR gas surrounding single AGN that also produce double peaked emission line profiles (e.g., Smith et al. 2012; Comerford & Greene 2014).

Satyapal et al. (2017) propose an alternative new method to search for dual AGN candidates based on the mid-infrared color $W_1 - W_2$ from the WISE survey (e.g., Wright et al. 2010). They argue that this method could discover the buried population of dual AGNs missed by optical observations. This method is highly powerful for luminous and highly obscured AGN systems, especially those systems including Type I AGNs (e.g., Hickox et al. 2017; Satyapal et al. 2017). However, this method may not be efficient at identifying dual AGNs composed of only Type II AGNs. In Fig. 13, we show the $W_1 - W_2$ color distribution of our dual AGN sample. The Type I AGN or dual AGN systems that contain at least one Type I AGN show redder $W_1 - W_2$ colors (> 0.6 mag) compared to typical values of stars and galaxies. In comparison, the dual AGNs that contain only Type II AGNs have a wide distribution of $W_1 - W_2$ colors, ranging from 0 to 1.0 mag that overlap significantly with those of stars or galaxies. In this sense, selection based on the mid-infrared color alone may exclude the dual AGN that only contain Type II AGNs and can not be used to construct a dual AGN sample without selection biases. But we note that those dual AGN candidates containing only Type II AGNs (especially those classified as Comp and Ambiguous AGN) in the current work require further solid confirmation (e.g., X-ray or radio follow-up observations). The method also suffers from the relatively low angular resolution of the WISE survey (Wright et al. 2010). As such, the yield of dual AGN sample from this method are all quite limited.

In addition, the systematic search for dual AGNs based on hard X-ray observations (e.g., Koss et al. 2011; Liu et al. 2013) and VLA Stripe 82 radio imaging (Fu et al. 2015) has

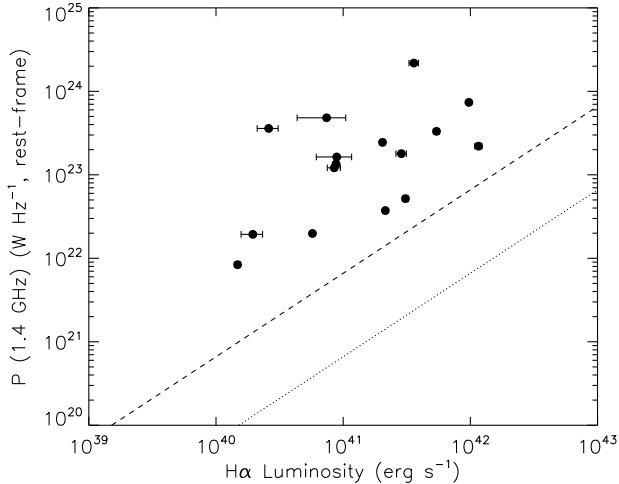


Figure 16. Rest-frame 1.4GHz radio power versus $H\alpha$ luminosity for the radio detected cores. Dotted line indicate radio-derived star formation rates (SFRs) equal to the $H\alpha$ -derived SFRs (using the relations from Hopkins et al. 2001), while the dashed line mark the former 10 times larger than the latter.

also been carried out. Restricted by the limited angular resolution and survey area, the number of dual AGNs thus identified is relatively less than theoretically predicted (e.g., Komossa & Zensus 2016). Higher angular resolution all-sky radio and X-ray surveys are required in the near future.

Here, we newly note that one system (J0907+5203; Fig. 14) in our dual AGN sample has two radio detections from the FIRST survey and their positions are in excellent agreement with the optical cores from the SDSS imaging. The radio detection of J0907+5203EN has a integrated flux density of 2.33 mJy with a typical RMS of 0.15 mJy¹⁶ given by the FIRST survey catalog (e.g., White et al. 1997). By assuming a general power law index¹⁷ of -0.7 , the luminosity of J0907+5203EN is $P_{1.4\text{GHz}} = 1.9 \times 10^{22} \text{ W Hz}^{-1}$. As the 1 mJy source detection threshold, the radio detection of J0907+5203WS doesn't have a integrated flux density in the FIRST survey catalog (e.g., White et al. 1997; Helfand, White & Becker 2015). Another one (J1214+2931; Fig. 15) shows two cores in the X-ray image obtained with the Chandra (also reported in Secrest et al. 2017) and their positions are again in line with the optical positions from the SDSS imaging. The dual AGN J1214+2931 is composed with a strong X-ray core (J1214+2931WS) and a weak X-ray core (J1214+2931EN) in 0.5-7 keV. The strong X-ray core (J1214+2931WS) is extremely luminous, with an intrinsic X-ray luminosity of $L_{2-10\text{keV}} = 4.0 \times 10^{43} \text{ erg s}^{-1}$. The weak X-ray core (J1214+2931EN) is only 2.6σ detection with only 7 counts in 0.5-2 keV. More detail information is described in Secrest et al. (2017).

In addition to the J0907+5203 system, the remaining 15 dual AGN candidates also have one radio detection from the FIRST catalog. The radio powers are then calculated for all the dual AGN candidates again assuming a power law index of -0.7 . To explore those radio radiation natures, the diagram between $P_{1.4\text{GHz}}$ and $L_{H\alpha}$ is shown in Fig. 16. The plot

¹⁶ <http://sundog.stsci.edu/index.html>

¹⁷ The assumed spectral index doesn't significantly affect the value of the radio luminosity given the small redshift (e.g., Pushkarev & Kovalev 2012, Hovatta et al. 2014).

clearly show that all the systems have radio powers over 10 times larger than those expected from the $H\alpha$ traced star formation rates, implying significant radio excesses from AGN activities. The results partly show that the candidates found in the current work are promising dual AGN systems.

To conclude, compared to the previous methods, the systematic method of searching for dual AGNs employed in the current work is relatively efficient, cost-effective, and capable to build a large sample of dual AGNs.

4.2. Potential applications of the sample

As mentioned earlier, this newly identified dual AGN sample, together with those known dual AGN in the literature, could provide vital information for understanding the co-evolution of SMBHs and their host galaxies. For example, by measuring the black hole masses and the velocity dispersions of the individual AGNs in those dual AGN systems, one can derive the $M_{\text{BH}}-\sigma$ relation for the dual AGN systems and test whether the relation is consistent with that found for normal galaxies and single AGNs (e.g., Komossa & Xu 2007; Fu et al. 2011a). In addition, one can explore the kinematics of gas and stellar components in those systems and investigate whether their behaviors are the same or not (e.g., Villforth & Hamann 2015; Zhang et al. 2016). In the forthcoming papers of this series, we will present results demonstrating the power of our dual AGN sample to understand the above issues.

5. CONCLUSION

Using an innovative method of systematically searching for and identifying dual-AGN systems amongst kpc scale merging galaxies, a total of 222 candidates are selected. As the first results of our ASTRO-DARING project, we have obtained long-slit spectroscopic observations for 41 targets between November 2014 and February 2017 using the YFOSC mounted on the LJT of Yunnan Observatories.

By careful data reduction, 1D spectra extraction, emission line profile fitting and AGN classification (based on the Balmer emission line widths and emission line ratios), 16 likely dual AGNs are finally identified (15 of them are found for the first time).

Our new searching approach is efficient (about 40 per cent, 16/41) and cost effective. With this new method, we plan to construct the current largest sample of dual AGNs (> 50) and better understand the co-evolution of host galaxies and their SMBHs.

ACKNOWLEDGEMENTS

We acknowledge the support of staff of the Lijiang 2.4-m telescope. Fund for the telescope has been provided by the Chinese Academy of Sciences and the People's Government of Yunnan Province. The work of J. M. Bai is supported by the NSFC (grants 11133006, 11361140347) and the Strategic Priority Research Program "The Emergence of Cosmological Structures" of the Chinese Academy of Sciences (grant No. XDB09000000). Y. Huang and X.-W. Liu acknowledge the supports by National Natural Science Foundation of China grants 11833006, 11811530289 and 11903027. It is a pleasure to thank Dr. Sarah Bird for a thorough read of the manuscript and improving the language significantly. We thank Hai-Cheng Feng, Kai-Xing Lu, Ding-Rong Xiong for assistance.

This work has made use of data products from the LJT (Lijiang 2.4-m telescope), SDSS, FIRST and WISE.

REFERENCES

- Abolfathi, B., Aguado, D. S., Aguilar, G., et al. 2018, *ApJS*, 235, 42
- Ahn, C. P. & et al. 2013, *VizieR Online Data Catalog*, V/139
- Alam, S., Albareti, F. D., Allende Prieto, C., et al. 2015, *ApJS*, 219, 12
- Azadi, M., Coil, A. L., Aird, J., et al. 2017, *ApJ*, 835, 27
- Baldwin, J. A., Phillips, M. M., & Terlevich, R. 1981, *PASP*, 93, 5
- Barrows, R. S., Sandberg Lacy, C. H., Kenefick, J., et al. 2013, *ApJ*, 769, 95
- Begelman M. C., Blandford R. D., Rees M. J., 1980, *Nature*, 287, 307
- Bell, E. F., Phleps, S., Somerville, R. S., et al. 2006, *ApJ*, 652, 270
- Blecha, L., Cox, T. J., Loeb, A., et al. 2011, *MNRAS*, 412, 2154
- Cappellari, M. & Emsellem, E. 2004, *PASP*, 116, 138
- Cappellari, M. 2017, *MNRAS*, 466, 798
- Cid Fernandes, R., Stasińska, G., Schlickmann, M. S., et al. 2010, *MNRAS*, 403, 1036
- Comerford, J. M., Pooley, D., Gerke, B. F., & Madejski, G. M. 2011, *ApJ*, 737, L19
- Comerford, J. M., Gerke, B. F., Stern, D., et al. 2012, *ApJ*, 753, 42
- Comerford, J. M., Schluns, K., Greene, J. E., & Cool, R. J. 2013, *ApJ*, 777, 64
- Comerford, J. M., & Greene, J. E. 2014, *ApJ*, 789, 112
- Comerford, J. M., Pooley, D., Barrows, R. S., et al. 2015, *ApJ*, 806, 219
- Colpi M., Dotti M., 2011, *ASdv. Sci. Lett.*, 4, 181
- Crenshaw, D. M., Fischer, T. C., Kraemer, S. B., et al. 2015, *ApJ*, 799, 83
- Das, M., Rubinur, K., Kharb, P., et al. 2018, *Bulletin de la Societe Royale des Sciences de Liege*, 87, 299
- Di Matteo, T., Springel, V., & Hernquist, L. 2005, *Nature*, 433, 604
- Ellison, S. L., Patton, D. R., Mendel, J. T., & Scudder, J. M. 2011, *MNRAS*, 418, 2043
- Ellison, S. L., Secrest, N. J., Mendel, J. T., et al. 2017, *MNRAS*, 470, L49
- Fan, Y.-F., Bai, J.-M., Zhang, J.-J., et al. 2015, *Research in Astronomy and Astrophysics*, 15, 918
- Ferrarese, L., & Merritt, D. 2000, *ApJ*, 539, L9
- Fu, H., Myers, A. D., Djorgovski, S. G., & Yan, L. 2011a, *ApJ*, 733, 103
- Fu, H., Zhang, Z.-Y., Assef, R. J., et al. 2011b, *ApJ*, 740, L44
- Fu, H., Yan, L., Myers, A. D., et al. 2012, *ApJ*, 745, 67
- Fu, H., Myers, A. D., Djorgovski, S. G., et al. 2015, *ApJ*, 799, 72
- Gabányi, K. É., Frey, S., Xiao, T., et al. 2014, *MNRAS*, 443, 1509
- Ge, J.-Q., Hu, C., Wang, J.-M., et al. 2012, *ApJS*, 201, 31
- Gebhardt, K., Bender, R., Bower, G., et al. 2000, *ApJ*, 539, L13
- Gerke, B. F., Newman, J. A., Lotz, J., et al. 2007, *ApJ*, 660, L23
- Graham, A. W., & Scott, N. 2013, *ApJ*, 764, 151
- Guainazzi, M., Piconcelli, E., Jiménez-Bailón, E., & Matt, G. 2005, *A&A*, 429, L9
- Gültekin, K., Richstone, D. O., Gebhardt, K., et al. 2009, *ApJ*, 698, 198
- Hao, L., Strauss, M. A., Tremonti, C. A., et al. 2005, *AJ*, 129, 1783
- Häring, N., & Rix, H.-W. 2004, *ApJ*, 604, L89
- Heckman, T. M. & Best, P. N. 2014, *ARA&A*, 52, 589
- Helfand, D. J., White, R. L., & Becker, R. H. 2015, *ApJ*, 801, 26
- Hennawi, J. F., Strauss, M. A., Oguri, M., et al. 2006, *AJ*, 131, 1
- Hennawi, J. F., Myers, A. D., Shen, Y., et al. 2010, *ApJ*, 719, 1672
- Hickox, R. C., Myers, A. D., Greene, J. E., et al. 2017, *ApJ*, 849, 53
- Hopkins, A. M., Connolly, A. J., Haarsma, D. B., et al. 2001, *AJ*, 122, 288
- Hopkins, P. F., Hernquist, L., Cox, T. J., et al. 2005, *ApJ*, 630, 705
- Hopkins P. F., Hernquist L., Cox T. J., Kereš D., 2008, *ApJS*, 175, 356
- Hovatta, T., Aller, M. F., Aller, H. D., et al. 2014, *AJ*, 147, 143
- Huang, Y., Liu, X.-W., Yuan, H.-B., et al. 2014, *MNRAS*, 439, 2927
- Hudson, D. S., Reiprich, T. H., Clarke, T. E., & Sarazin, C. L. 2006, *A&A*, 453, 433
- Jogee, S., Miller, S. H., Penner, K., et al. 2009, *ApJ*, 697, 1971
- Kauffmann, G., & Haehnelt, M. 2000, *MNRAS*, 311, 576
- Kauffmann, G., Heckman, T. M., Tremonti, C., et al. 2003, *MNRAS*, 346, 1055
- Kauffmann, G. & Heckman, T. M. 2009, *MNRAS*, 397, 135
- Kewley, L. J., Dopita, M. A., Sutherland, R. S., Heisler, C. A., & Trevena, J. 2001, *ApJ*, 556, 121
- Kewley, L. J., Groves, B., Kauffmann, G., & Heckman, T. 2006, *MNRAS*, 372, 961
- Kocevski, D. D., Faber, S. M., Mozena, M., et al. 2012, *ApJ*, 744, 148
- Kormendy, J., & Ho, L. C. 2013, *ARA&A*, 51, 511
- Kormendy, J., & Richstone, D. 1995, *ARA&A*, 33, 581
- Komossa S., Burwitz V., Hasinger G., Predehl P., Kaastra J. S., Ikebe Y., 2003, *ApJ*, 582L, 15
- Komossa, S., & Xu, D. 2007, *ApJ*, 667, L33
- Komossa, S., & Zensus, J. A. 2016, in *IAU Symposium*, Vol. 312, IAU Symposium, ed. Y. Meiron, S. Li, F.-K. Liu, & R. Spurzem, 13–25
- Kosec, P., Brightman, M., Stern, D., et al. 2017, *ApJ*, 850, 168
- Koss, M., et al. 2011, *ApJ*, 735, L42
- Koss, M., Mushotzky, R., Treister, E., et al. 2012, *ApJ*, 746, L22
- Koss, M. J., Glidden, A., Baloković, M., et al. 2016, *ApJ*, 824, L4
- Liu, X., Shen, Y., Strauss, M. A., et al. 2010a, *apj*, 708, 427
- Liu, X., Greene, J. E., Shen, Y., & Strauss, M. A. 2010b, *apj*, 715, L30
- Liu, X., Shen, Y., Strauss, M. A., & Hao, L. 2011, *ApJ*, 737, 101
- Liu, X., Civano, F., Shen, Y., et al. 2013, *ApJ*, 762, 110
- McConnell, N. J., & Ma, C.-P. 2013, *ApJ*, 764, 184
- McGurk, R. C., Max, C. E., Rosario, D. J., Shields, G. A., Smith, K. L., & Wright, S. A. 2011, *ApJ*, 738, L2
- McGurk, R. C., Max, C. E., Medling, A. M., Shields, G. A., & Comerford, J. M. 2015, *ApJ*, 811, 14
- Milosavljević M., Merritt, D., 2001, *ApJ*, 563, 34
- Müller-Sánchez, F., Comerford, J. M., Nevin, R., et al. 2015, *ApJ*, 813, 103
- Müller-Sánchez, F., Comerford, J., Stern, D., et al. 2016, *ApJ*, 830, 50
- Netzer, H. 2015, *ARA&A*, 53, 365
- Nevin, R., Comerford, J., Müller-Sánchez, F., Barrows, R., & Cooper, M. 2016, *ApJ*, 832, 67
- Nevin, R., Comerford, J. M., Müller-Sánchez, F., et al. 2018, *MNRAS*, 473, 2160
- Pâris, I., Petitjean, P., Ross, N. P., et al. 2017, *A&A*, 597, A79.
- Pâris, I., Petitjean, P., Aubourg, É., et al. 2018, *A&A*, 613, A51
- Pushkarev, A. B. & Kovalev, Y. Y. 2012, *A&A*, 544, A34
- Ricci, F., La Franca, F., Marconi, A., et al. 2017, *MNRAS*, 471, L41
- Richstone, D., Ajhar, E. A., Bender, R., et al. 1998, *Nature*, 395, A14
- Rodriguez, C., Taylor, G. B., Zavala, R. T., et al. 2006, *ApJ*, 646, 49
- Robaina, A. R., Bell, E. F., Skelton, R. E., et al. 2009, *ApJ*, 704, 324
- Rosario D. J., McGurk R. C., Max C. E., Shields G. A., Smith K. L., Ammons S. M., 2011, *ApJ*, 739, 44
- Rubinur, K., Das, M., Kharb, P., & Honey, M. 2017, *MNRAS*, 465, 4772
- Rubinur, K., Das, M., & Kharb, P. 2019, *MNRAS*, 484, 4933
- Sánchez-Blázquez, P., Peletier, R. F., Jiménez-Vicente, J., et al. 2006, *MNRAS*, 371, 703
- Sanders, D. B., Scoville, N. Z., & Soifer, B. T. 1988, *ApJ*, 335, L1
- Satyapal, S., Ellison, S. L., McAlpine, W., et al. 2014, *MNRAS*, 441, 1297
- Satyapal, S., Secrest, N. J., Ricci, C., et al. 2017, *ApJ*, 848, 126
- Savognan, G. A. D., & Graham, A. W. 2015, *MNRAS*, 446, 2330
- Secrest, N. J., Schmitt, H. R., Blecha, L., Rothberg, B., & Fischer, J. 2017, *ApJ*, 836, 183
- Shen, Y., Liu, X., Greene, J. E., & Strauss, M. A. 2011, *ApJ*, 735, 48
- Sheinis, A. I. & López-Sánchez, Á. R. 2017, *AJ*, 153, 55
- Shi, Z.-X., Luo, A.-L., Comte, G., et al. 2014, *Research in Astronomy and Astrophysics*, 14, 1234-1250
- Smith, K. L., Shields, G. A., Bonning, E. W., et al. 2010, *ApJ*, 716, 866
- Smith, K. L., Shields, G. A., Salviander, S., Stevens, A. C., & Rosario, D. J. 2011, *ArXiv e-prints* 1108.0383
- Smith, K. L., Shields, G. A., Salviander, S., et al. 2012, *ApJ*, 752, 63
- Solanes, J. M., Perea, J. D., Valentí-Rojas, G., et al. 2019, *A&A*, 624, A86
- Stern, J. & Laor, A. 2013, *MNRAS*, 431, 836
- Treister, E., Schawinski, K., Urry, C. M., et al. 2012, *ApJ*, 758, L39
- Veilleux, S., & Osterbrock, D. E. 1987, *ApJS*, 63, 295
- Villforth, C., & Hamann, F. 2015, *AJ*, 149, 92
- Volonteri, M., Haardt, F., & Madau, P. 2003, *ApJ*, 582, 559
- Wang, J.-M., Chen, Y.-M., Hu, C., et al. 2009, *ApJ*, 705, L76
- White, R. L., Becker, R. H., Helfand, D. J., et al. 1997, *ApJ*, 475, 479
- Wright, E. L., Eisenhardt, P. R. M., Mainzer, A. K., et al. 2010, *AJ*, 140, 1868
- Yu Q. -J., Lu Y. -J., Mohayaee R., Colin, J., 2011, *ApJ*, 738, 92
- Zhang, Y.-W., Huang, Y., Bai, J.-M., Liu, X.-W., & Wang, J.-G. 2016, *Research in Astronomy and Astrophysics*, 16, 41
- Zhou, H., Wang, T., Zhang, X., Dong, X., & Li, C. 2004, *ApJ*, 604, L33

APPENDIX

A. FWHM OF WELL DETECTED EMISSION LINES

Table A1

Name	FWHM	FWHM	FWHM	FWHM	FWHM	FWHM	FWHM	FWHM	FWHM
Emission line	H β	[O III] λ 4959	[O III] λ 5007	[O I] λ 6300	[N II] λ 6549	H α	[N II] λ 6583	[S II] λ 6717	[S II] λ 6731
First phase (6 Dual AGNs)									
J0151-0245WN	204 \pm 88	221 \pm 77	262 \pm 63	495 \pm 21	177 \pm 63	257 \pm 39	344 \pm 32	456 \pm 27	396 \pm 31
J0151-0245ES	259 \pm 69	211 \pm 102	471 \pm 36	557 \pm 55	562 \pm 25	213 \pm 51	416 \pm 23	704 \pm 35	621 \pm 38
J0933+2114EN	192 \pm 99	525 \pm 58	629 \pm 46	555 \pm 47	566 \pm 43	519 \pm 34	588 \pm 31	660 \pm 47	382 \pm 68
J0933+2114WS	522 \pm 59	545 \pm 55	548 \pm 53	404 \pm 54	541 \pm 36	449 \pm 38	758 \pm 23	365 \pm 50	240 \pm 78
J1017+3448NW	899 \pm 47	736 \pm 63	778 \pm 41	779 \pm 178	509 \pm 43	368 \pm 47	392 \pm 44	590 \pm 27	395 \pm 41
J1017+3448SE	514 \pm 77	406 \pm 75	614 \pm 48	179 \pm 122	468 \pm 66	486 \pm 39	425 \pm 43	110 \pm 165	91 \pm 57
J1105+1957EN	131 \pm 55	261 \pm 57	487 \pm 46	413 \pm 22	516 \pm 37	236 \pm 35	292 \pm 28	400 \pm 20	246 \pm 32
J1105+1957WS	450 \pm 47	120 \pm 78	399 \pm 50	428 \pm 27	480 \pm 27	378 \pm 22	332 \pm 25	486 \pm 36	321 \pm 24
J1633+4718N	680 \pm 48	333 \pm 94	413 \pm 71	466 \pm 54	121 \pm 83	284 \pm 60	303 \pm 56	316 \pm 51	294 \pm 55
J1633+4718S	772 \pm 41	317 \pm 95	517 \pm 57	591 \pm 40	132 \pm 68	496 \pm 36	355 \pm 49	339 \pm 50	369 \pm 47
J2258-0115EN	711 \pm 48	405 \pm 96	738 \pm 43	406 \pm 54	326 \pm 57	539 \pm 31	481 \pm 35	615 \pm 37	473 \pm 37
J2258-0115WS	624 \pm 55	790 \pm 38	650 \pm 46	634 \pm 33	519 \pm 33	369 \pm 47	397 \pm 43	340 \pm 51	164 \pm 61
Second phase (10 Dual AGNs)									
J0217-0845EN	548 \pm 213	512 \pm 224	339 \pm 237	573 \pm 153	244 \pm 173	483 \pm 164	344 \pm 206	308 \pm 238	605 \pm 119
J0217-0845WS	657 \pm 178	641 \pm 175	670 \pm 164	651 \pm 149	193 \pm 166	418 \pm 162	402 \pm 164	479 \pm 139	147 \pm 132
J0756+2340EN	780 \pm 150	718 \pm 160	806 \pm 151	622 \pm 115	617 \pm 105	604 \pm 106	554 \pm 115	536 \pm 115	546 \pm 111
J0756+2340WS	728 \pm 161	731 \pm 159	565 \pm 195	563 \pm 129	490 \pm 136	454 \pm 142	419 \pm 152	568 \pm 123	531 \pm 116
J0813+4941WN	525 \pm 245	709 \pm 162	804 \pm 138	575 \pm 278	434 \pm 149	383 \pm 173	381 \pm 168	617 \pm 100	589 \pm 104
J0813+4941ES	458 \pm 255	795 \pm 153	521 \pm 212	648 \pm 114	334 \pm 276	616 \pm 104	691 \pm 192	615 \pm 199	563 \pm 115
J0833+1532WN	379 \pm 249	391 \pm 297	427 \pm 285	508 \pm 138	380 \pm 138	466 \pm 159	733 \pm 165	450 \pm 139	296 \pm 151
J0833+1532ES	561 \pm 210	535 \pm 210	486 \pm 227	771 \pm 190	702 \pm 194	611 \pm 107	477 \pm 144	494 \pm 124	418 \pm 146
J0848+3515EN	352 \pm 238	631 \pm 179	496 \pm 272	367 \pm 172	475 \pm 136	398 \pm 224	384 \pm 250	609 \pm 100	299 \pm 136
J0848+3515WS	545 \pm 215	370 \pm 203	498 \pm 221	599 \pm 117	437 \pm 149	544 \pm 117	619 \pm 103	515 \pm 118	515 \pm 118
J0907+5203EN	761 \pm 118	821 \pm 104	815 \pm 102	420 \pm 127	696 \pm 171	623 \pm 178	369 \pm 178	538 \pm 114	511 \pm 190
J0907+5203WS	581 \pm 162	702 \pm 121	709 \pm 117	485 \pm 119	277 \pm 208	455 \pm 108	543 \pm 162	494 \pm 194	463 \pm 199
J1214+2931EN	371 \pm 242	490 \pm 230	576 \pm 191	588 \pm 119	398 \pm 216	586 \pm 144	332 \pm 191	444 \pm 139	611 \pm 100
J1214+2931WS	556 \pm 156	683 \pm 164	648 \pm 170	430 \pm 164	550 \pm 199	562 \pm 114	398 \pm 161	445 \pm 137	535 \pm 117
J1645+2057WN	511 \pm 111	524 \pm 103	644 \pm 85	443 \pm 74	210 \pm 159	280 \pm 126	856 \pm 80	212 \pm 150	175 \pm 106
J1645+2057ES	668 \pm 199	526 \pm 124	833 \pm 64	547 \pm 63	359 \pm 151	386 \pm 101	521 \pm 58	280 \pm 123	378 \pm 83
J2206+0003WN	777 \pm 175	376 \pm 257	889 \pm 157	407 \pm 144	581 \pm 96	342 \pm 102	165 \pm 118	243 \pm 127	384 \pm 118
J2206+0003ES	255 \pm 237	757 \pm 178	650 \pm 185	293 \pm 190	342 \pm 98	353 \pm 123	592 \pm 55	268 \pm 118	110 \pm 79
J2314+0653WN	680 \pm 187	427 \pm 132	393 \pm 141	449 \pm 178	613 \pm 56	270 \pm 119	189 \pm 107	207 \pm 149	251 \pm 122
J2314+0653ES	232 \pm 162	880 \pm 179	419 \pm 133	313 \pm 134	374 \pm 87	295 \pm 109	370 \pm 186	461 \pm 167	265 \pm 197

Notes: FWHM in units of km s^{-1} . The FWHMs of H β and H α emission lines are both for the narrow line component. The FWHM of H α broad line component shown in Table 5.

B. NOTES FOR INDIVIDUAL DUAL AGNS

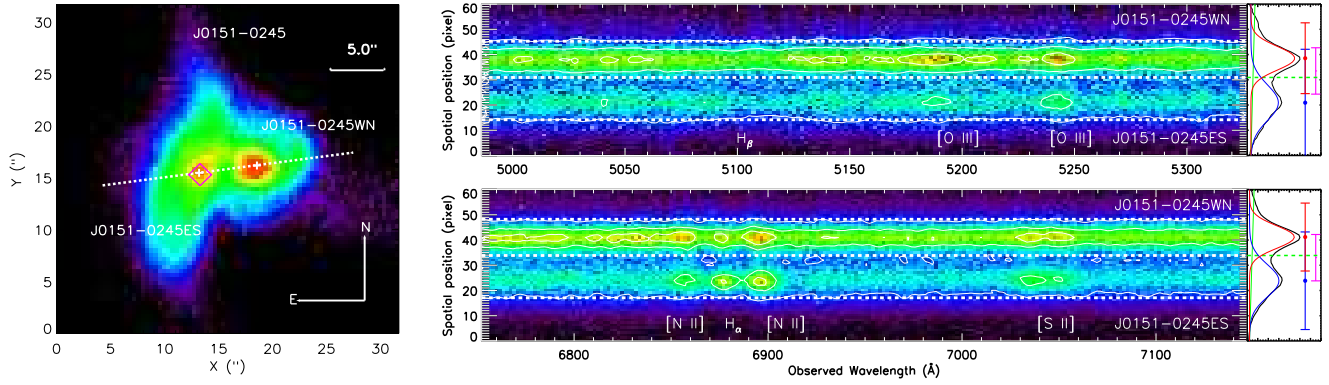


Figure B1. Same as Fig. 1 but for J0151-0245. The spectra from LJT.

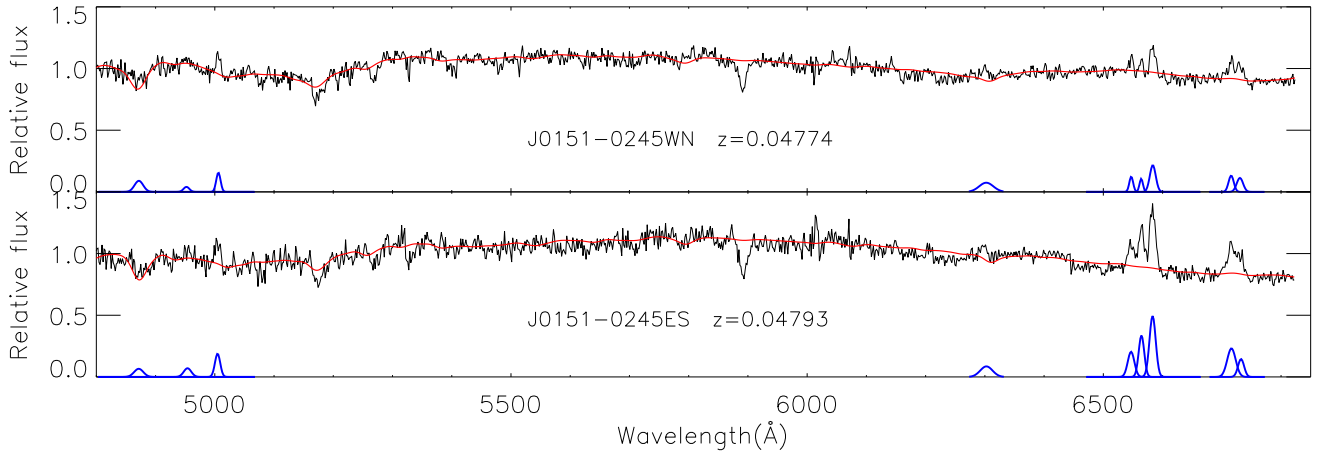


Figure B2. Same as Fig. 3 but for J0151-0245.

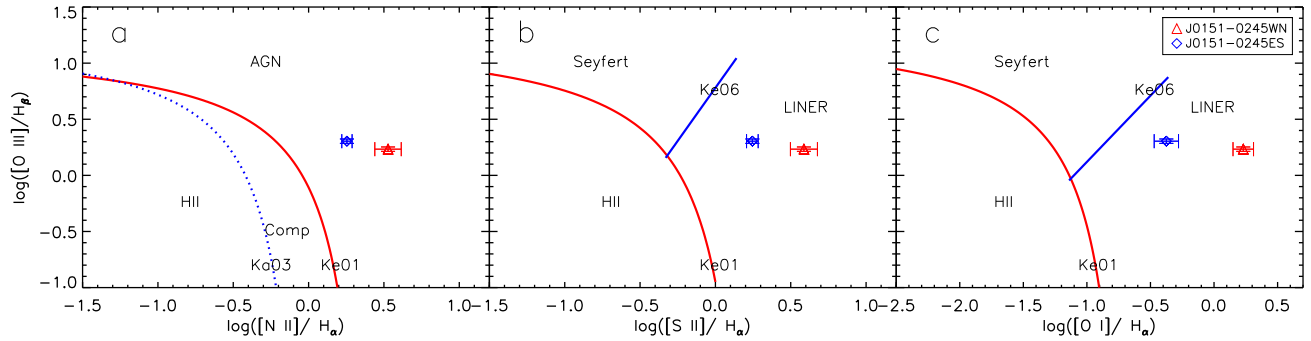


Figure B3. Same as Fig. 5 but for J0151-0245.

DUAL AGN: J015107.39-024526.87

Two sets of AGN spectra are spatially resolved as shown in Fig. B1, so the two cores, i.e. J0151-0245WN and J0151-0245ES can be identified separately.

The fitting of extracted 1D spectra of the two cores are shown in Fig. B2. The redshifts, FWHMs of emission lines and emission line flux ratios of the two cores, measured from the 1D spectra, are presented in Tables 4 and 5. For the two cores, no broad line components are detected, we therefore use BPT diagram to classify their types (Fig. B3). According to the diagnosis, both cores are classified as LINER.

The object J015107.39-024526.87 has been revealed as a dual AGN composed of two LINERs. This dual AGN has a separation of 4.8 kpc and a velocity offset of $57 \pm 28 \text{ km s}^{-1}$.

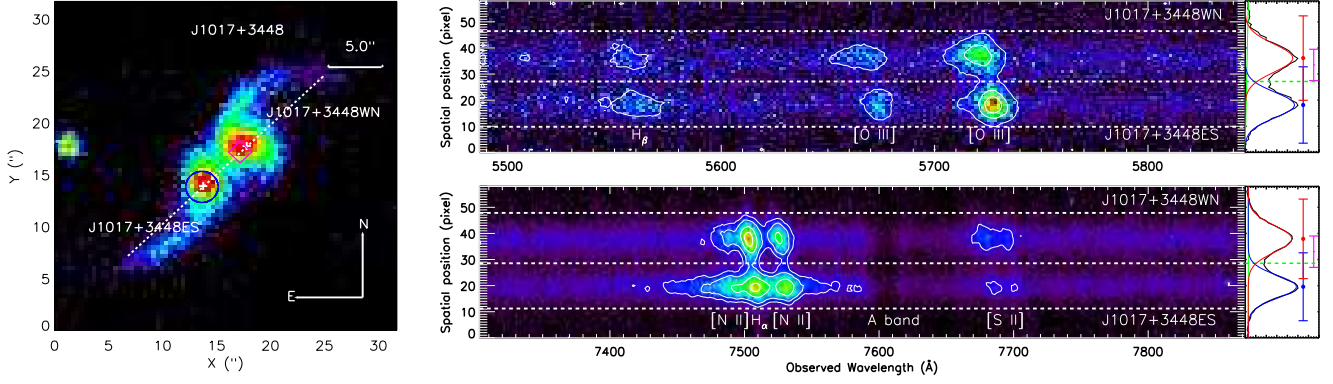


Figure B4. Same as Fig. 1 but for J1017+3448.

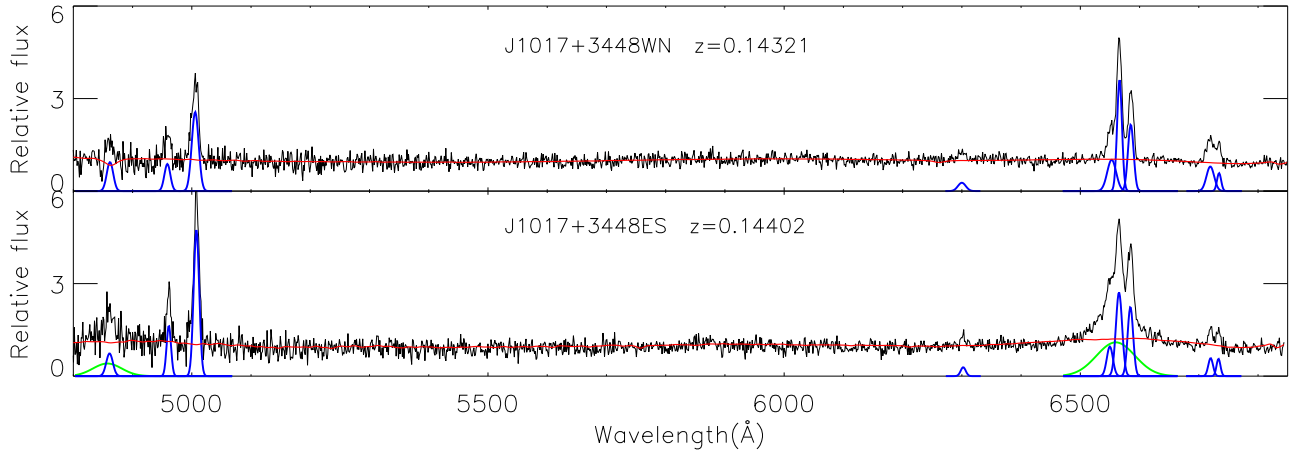


Figure B5. Same as Fig. 3 but for J1017+3448. The spectra from LJT.

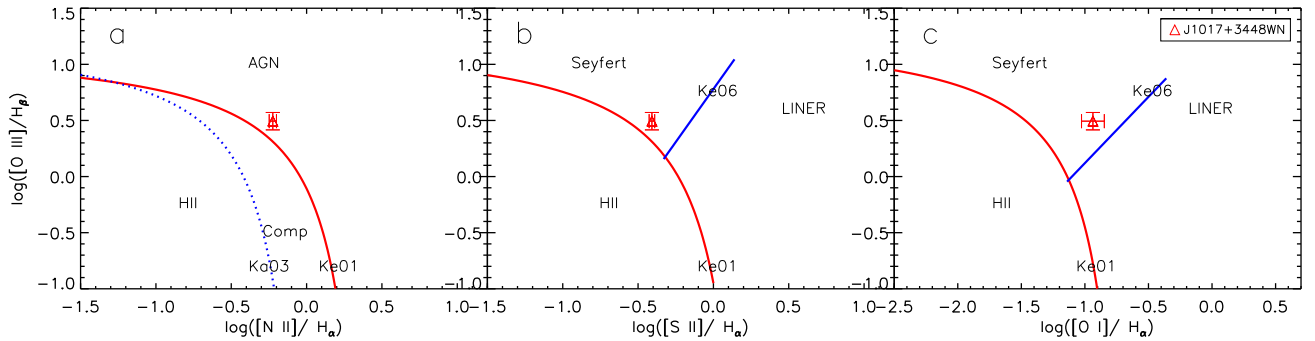


Figure B6. Same as Fig. 5 but for J1017+3448.

DUAL AGN: J101757.07+344846.61

Two sets of AGN spectra are spatially resolved as shown in Fig. B4, so the two cores, i.e. J1017+3448WN and J1017+3448ES can be identified separately.

The fitting of extracted 1D spectra of the two cores are shown in Fig. B5. The redshifts, FWHMs of emission lines and emission line flux ratios of the two cores, measured from the 1D spectra, are presented in Tables 4 and 5. The spectrum of J1017+3448WN does not show a broad line (Fig. B5). We use the BPT diagram to distinguish this AGN shown in Fig. B6. It is classified as a Seyfert (AGN). The spectrum of J1017+3448ES has broad line (Fig. B5, $\text{FWHM} > 2000 \text{ km s}^{-1}$ as measured from $\text{H}\alpha$ broad line component) and thus it is a Type I AGN.

The object J101757.07+344846.61 has been revealed as a dual AGN composed of Seyfert (J1017+3448WN) and Type I AGN (J1017+3448ES). This dual AGN has a separation of 14.2 kpc and a velocity offset of $243 \pm 21 \text{ km s}^{-1}$.

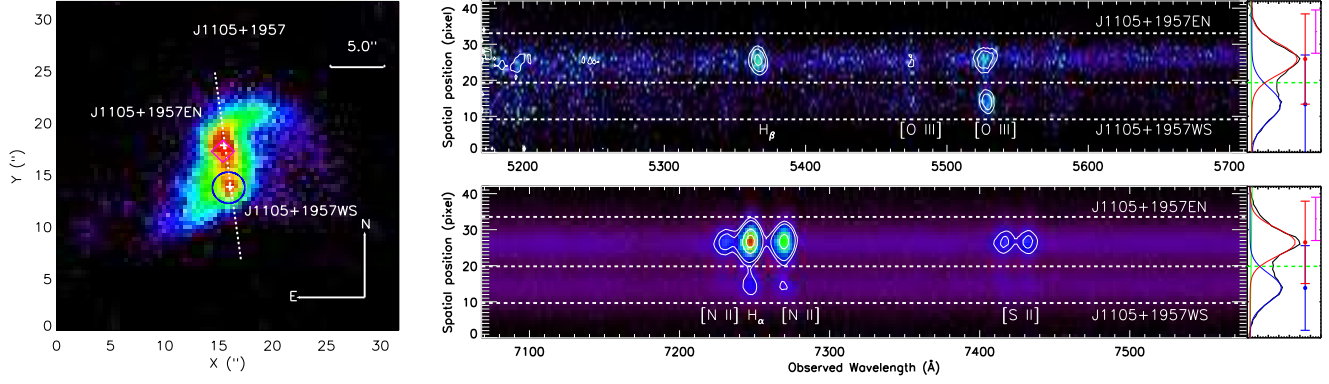


Figure B7. Same as Fig. 1 but for J1105+1957.

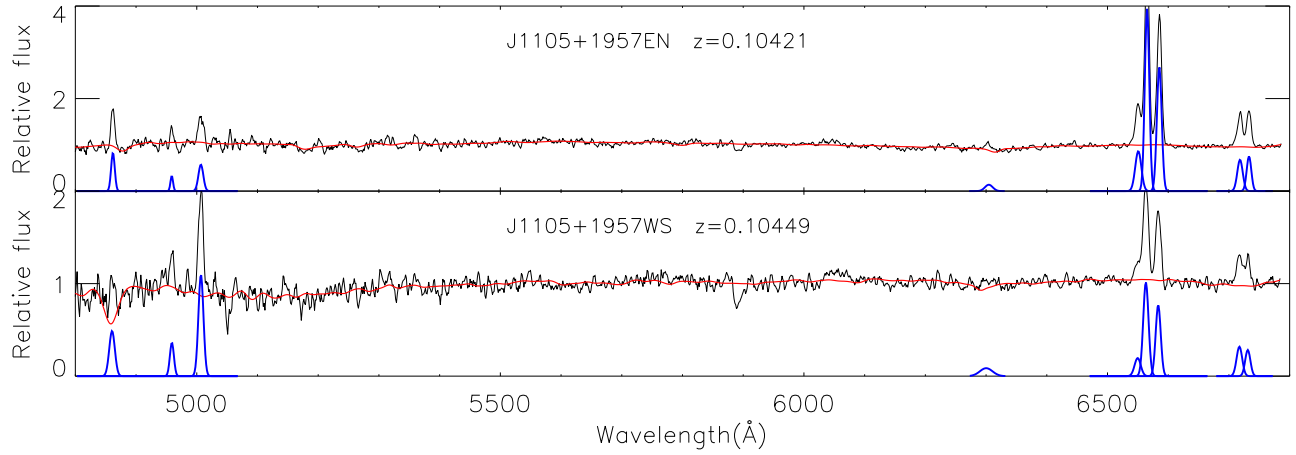


Figure B8. Same as Fig. 3 but for J1105+1957. The spectra from LJT.

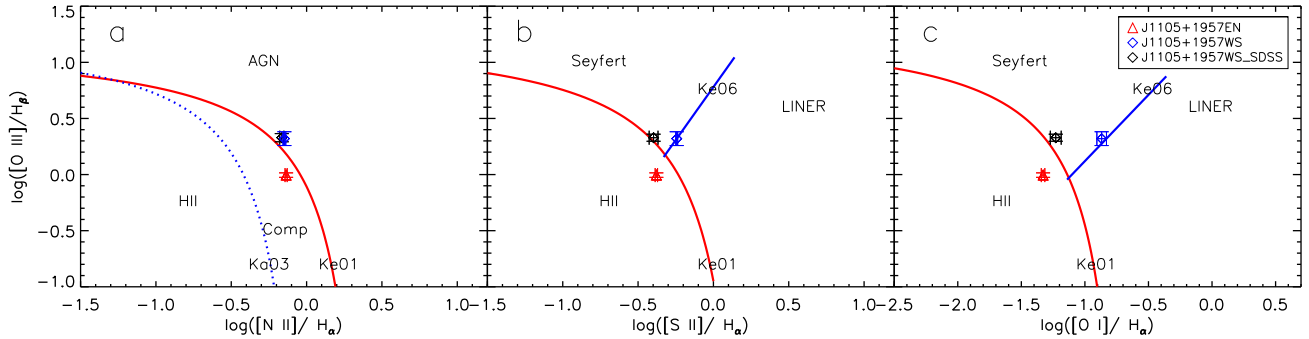


Figure B9. Same as Fig. 5 but for J1105+1957.

DUAL AGN: J110544.48+195750.06

Two sets of AGN spectra are spatially resolved as shown in Fig. B7, so the two cores, i.e. J1105+1957EN and J1105+1957WS can be identified separately.

The fitting of extracted 1D spectra of the two cores are shown in Fig. B8. The redshifts, FWHMs of emission lines and emission line flux ratios of the two cores, measured from the 1D spectra, are presented in Tables 4 and 5. For the two cores, no broad line components are detected, we therefore use BPT diagram to classify their types (Fig. B9). According to the diagnosis, J1105+1957EN is classified as Comp (AGN) and J1105+1957WS is classified as Seyfert (AGN).

The object J110544.48+195750.06 has been revealed as a dual AGN composed of ambiguous galaxy (AGN) (J1105+1957EN) and Seyfert (J1105+1957WS). This dual AGN has a separation of 7.4 kpc and a velocity offset of $84 \pm 21 \text{ km s}^{-1}$.

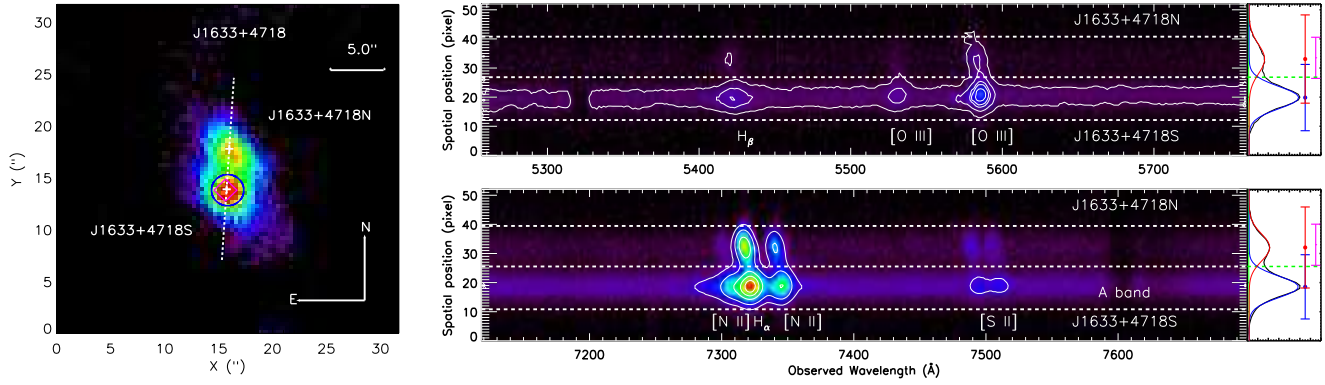


Figure B10. Same as Fig. 1 but for J1633+4718.

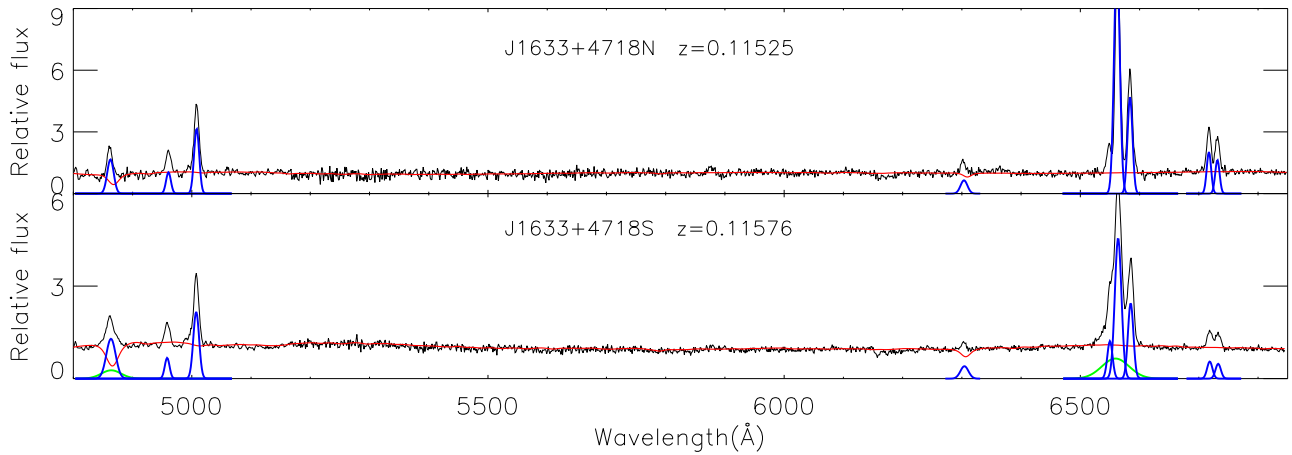


Figure B11. Same as Fig. 3 but for J1633+4718. The spectra from LJT.

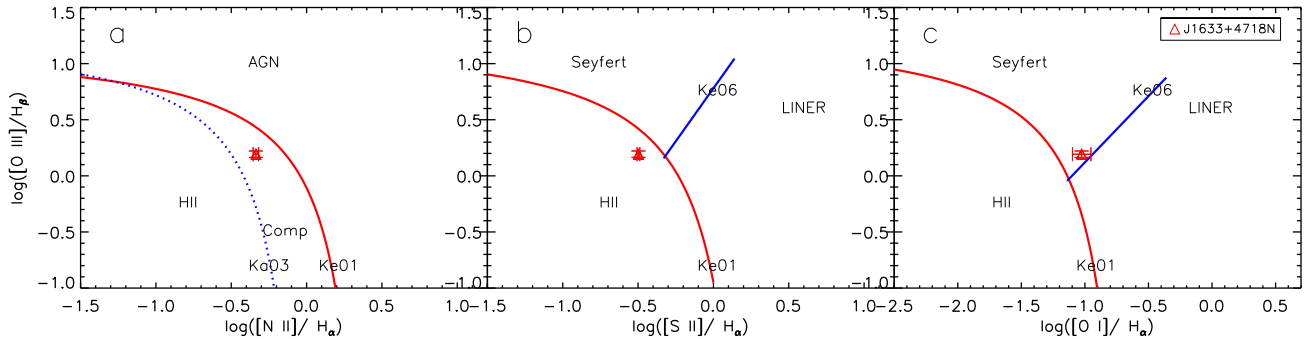


Figure B12. Same as Fig. 5 but for J1633+4718.

DUAL AGN: J163323.58+471858.95

Two sets of AGN spectra are spatially resolved as shown in Fig. B10, so the two cores, i.e. J1633+4718N and J1633+4718S can be identified separately.

The fitting of extracted 1D spectra of the two cores are shown in Fig. B11. The redshifts, FWHMs of emission lines and emission line flux ratios of the two cores, measured from the 1D spectra, are presented in Tables 4 and 5. The spectrum of J1633+4718N doesn't show a broad line (Fig. B11). We use the BPT diagram to distinguish this AGN shown in Fig. B12. The J1633+4718N is revealed as ambiguous galaxy (AGN). The spectrum of J1633+4718S has broad line (Fig. B11). The FWHM of the BLR is $1965 \pm 66 \text{ km s}^{-1}$ that measured from the $H\alpha$ broad line component and $h(\text{Hbroad})/h(\text{Hnarrow})$ is 0.29 (> 0.1). According to Hao et al. (2005), J1633+4718S is a Type I AGN.

The object J163323.58+471858.95 has been revealed as a dual AGN composed of ambiguous galaxy (AGN) (J1633+4718N) and Type I AGN (J1633+4718S). This dual AGN has a separation of 8.0 kpc and a velocity offset of $153 \pm 21 \text{ km s}^{-1}$.

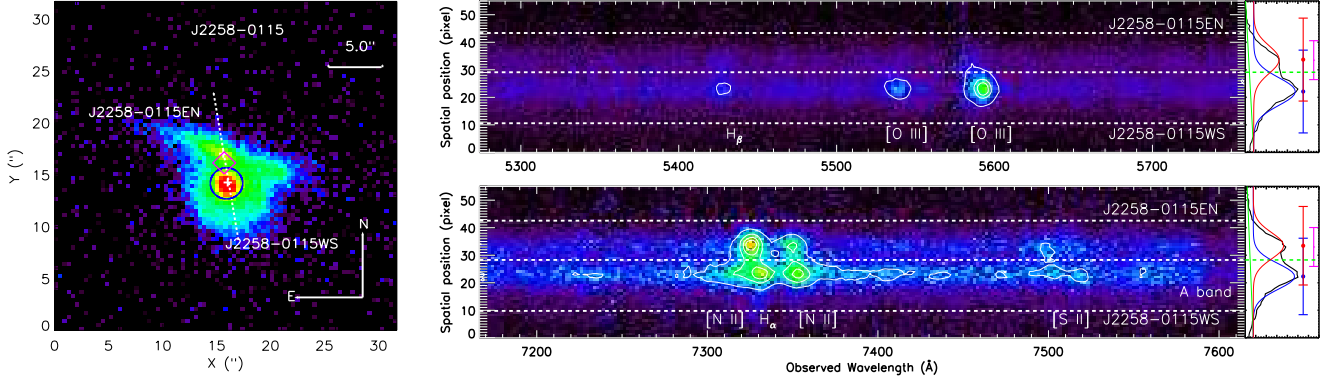


Figure B13. Same as Fig. 1 but for J2258-0115.

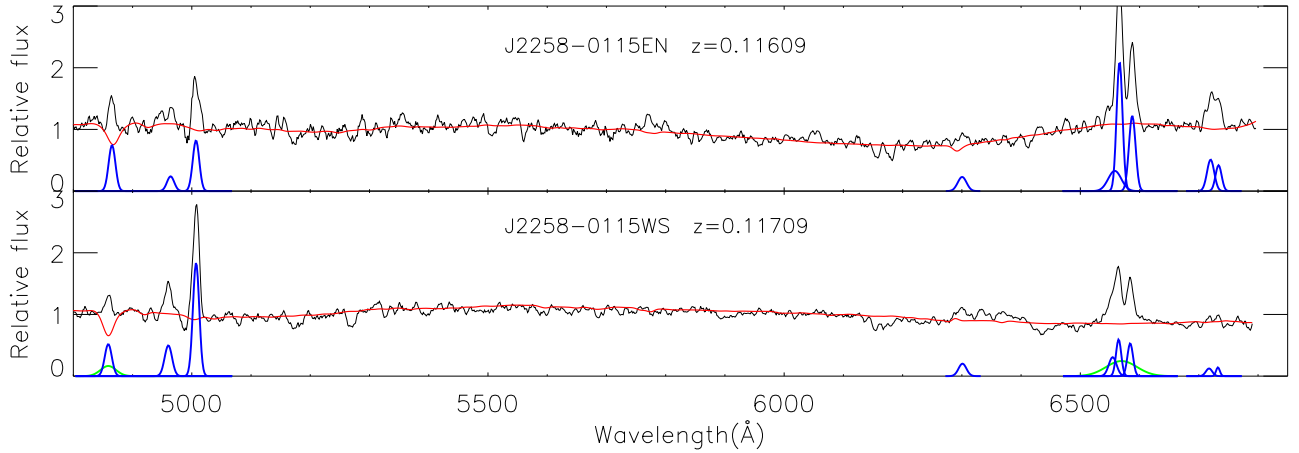


Figure B14. Same as Fig. 3 but for J2258-0115. The spectra from LJT.

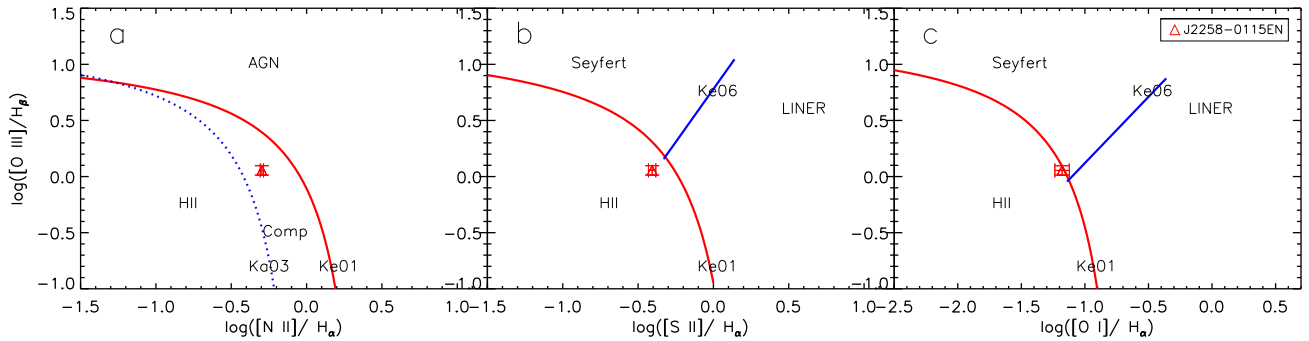


Figure B15. Same as Fig. 5 but for J2258-0115.

DUAL AGN: J225810.01-011516.26

Two sets of AGN spectra are spatially resolved as shown in Fig. B13, so the two cores, i.e. J2258–0115EN and J2258–0115WS can be identified separately.

The fitting of extracted 1D spectra of the two cores are shown in Fig. B14. The redshifts, FWHMs of emission lines and emission line flux ratios of the two cores, measured from the 1D spectra, are presented in Tables 4 and 5. The spectrum of J2258–0115EN doesn't show a broad line (Fig. B14). We use the BPT diagram to distinguish this AGN shown in Fig. B15 and it is classified as Comp (AGN). The spectrum of J2258–0115WS has broad line (Fig. B14, FWHM $> 2000 \text{ km s}^{-1}$ as measured from $H\alpha$ broad line component) and thus it is a Type I AGN.

The object J225810.01-011516.26 has been revealed as a dual AGN composed of ambiguous galaxy (AGN) (J2258–0115EN) and Type I AGN (J2258–0115WS). This dual AGN has a separation of 6.9 kpc and a velocity offset of $300 \pm 21 \text{ km s}^{-1}$.

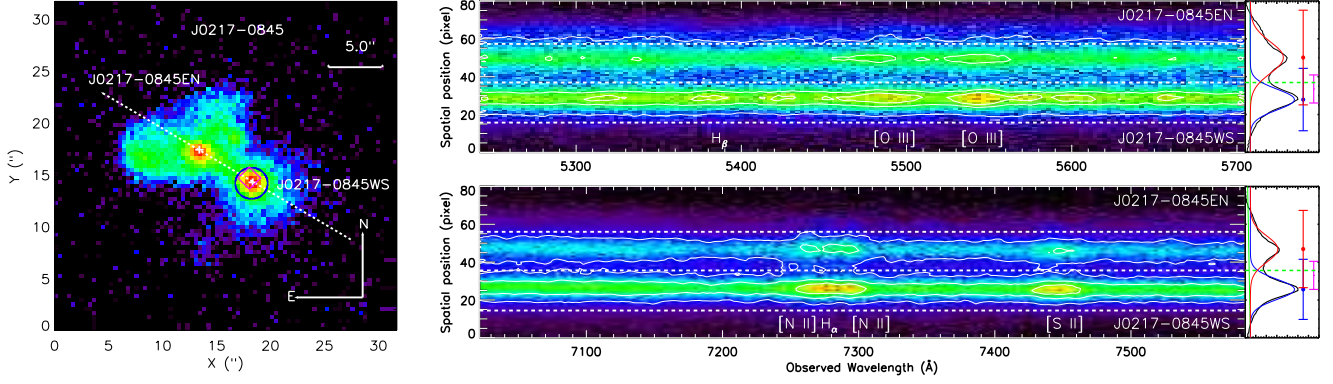


Figure B16. Same as Fig. 1 but for J0217-0845.

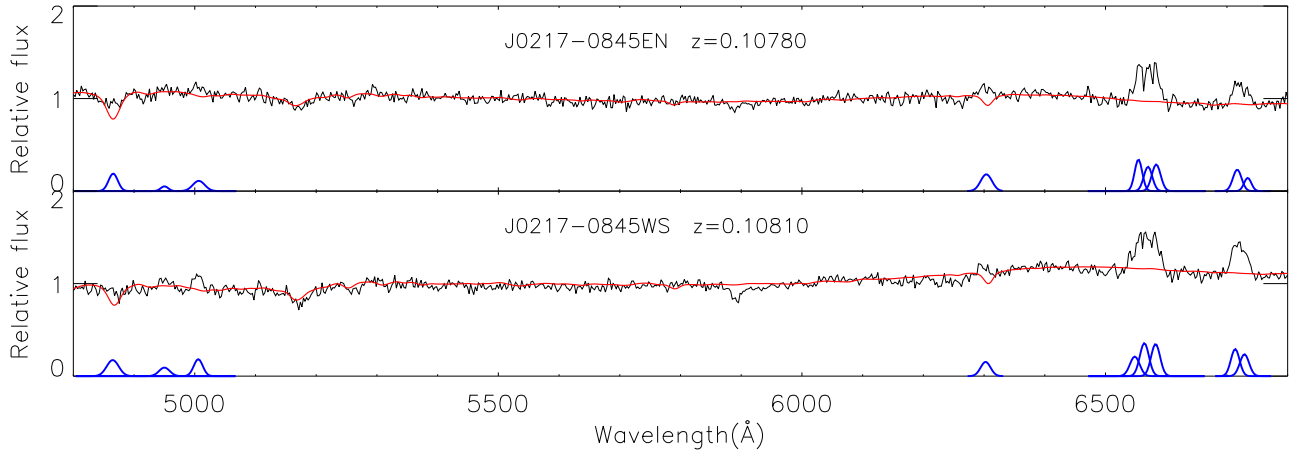


Figure B17. Same as Fig. 3 but for J0217-0845. The spectra from LJT.

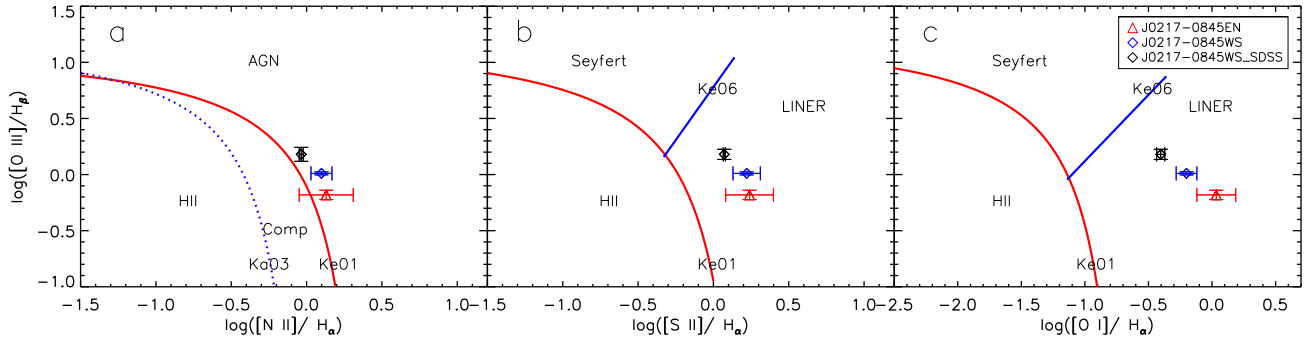


Figure B18. Same as Fig. 5 but for J0217-0845.

DUAL AGN: J021703.81-084515.97

Two sets of AGN spectra are spatially resolved as shown in Fig. B16, so the two cores, i.e. J0217-0845EN and J0217-0845WS can be identified separately.

The fitting of extracted 1D spectra of the two cores are shown in Fig. B17. The redshifts, FWHMs of emission lines and emission line flux ratios of the two cores, measured from the 1D spectra, are presented in Tables 4 and 5. For the two cores, no broad line components are detected, we therefore use BPT diagram to classify their types (Fig. B18). According to the diagnosis, both cores are classified as LINER.

The object J021703.81-084515.97 has been revealed as a dual AGN composed of LINER (J0217-0845EN) and LINER (J0217-0845WS). This dual AGN has a separation of 12.0 kpc and a velocity offset of $90 \pm 40 \text{ km s}^{-1}$.

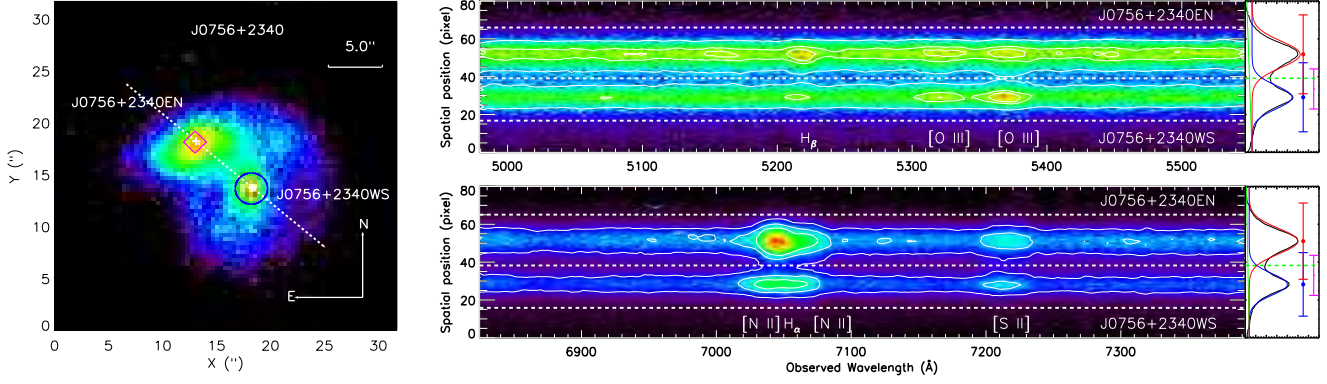


Figure B19. Same as Fig. 1 but for J0756+2340.

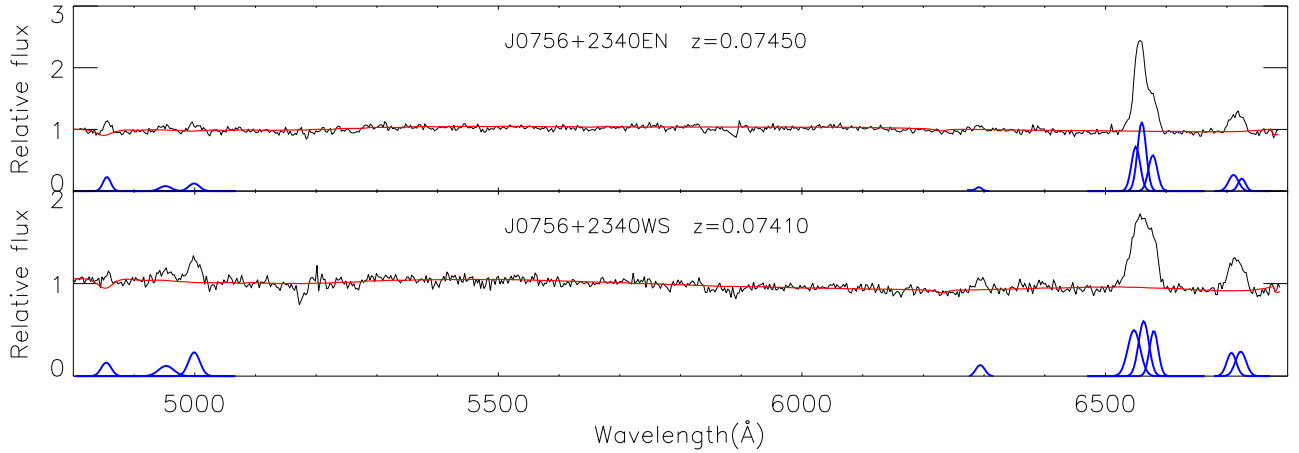


Figure B20. Same as Fig. 3 but for J0756+2340. The spectra from LJT.

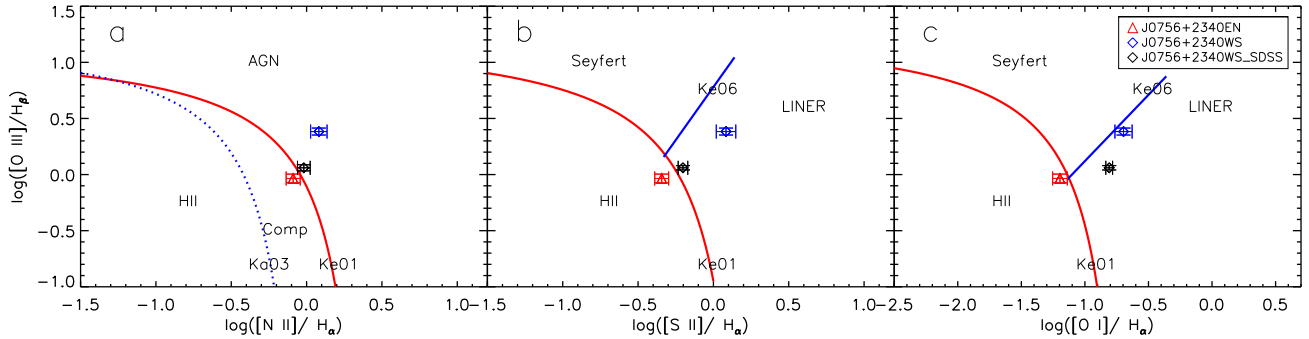


Figure B21. Same as Fig. 5 but for J0756+2340.

DUAL AGN: J075621.37+234043.97

Two sets of AGN spectra are spatially resolved as shown in Fig. B19, so the two cores, i.e. J0756+2340EN and J0756+2340WS can be identified separately.

The fitting of extracted 1D spectra of the two cores are shown in Fig. B20. The redshifts, FWHMs of emission lines and emission line flux ratios of the two cores, measured from the 1D spectra, are presented in Tables 4 and 5. For the two cores, no broad line components are detected, we therefore use BPT diagram to classify their types (Fig. B21). According to the diagnosis, J0756+2340EN is classified as Comp (AGN) and J0756+2340WS is classified as LINER (AGN).

The object J075621.37+234043.97 has been revealed as a dual AGN composed of ambiguous AGN (J0756+2340EN) and LINER (J0756+2340WS). This dual AGN has a separation of 9.6 kpc and a velocity offset of $120 \pm 40 \text{ km s}^{-1}$.

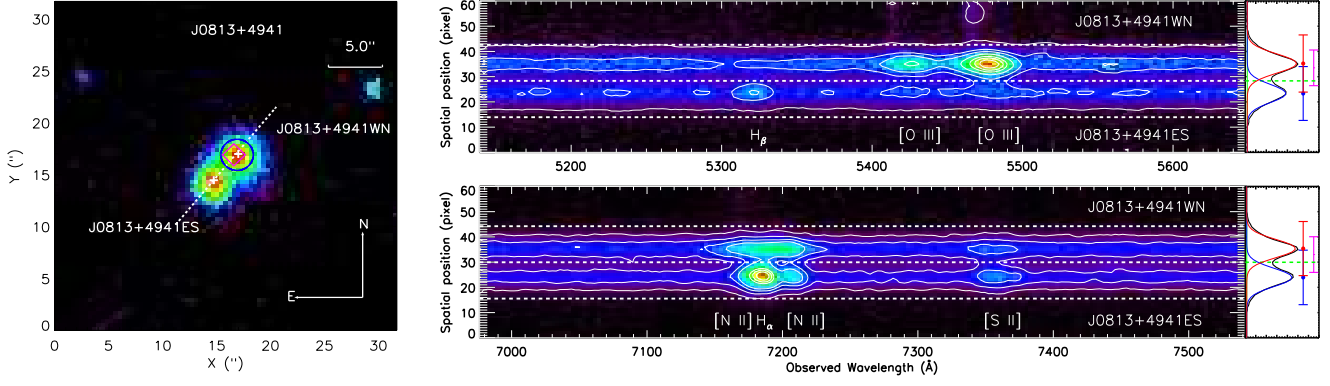


Figure B22. Same as Fig. 1 but for J0813+4941.

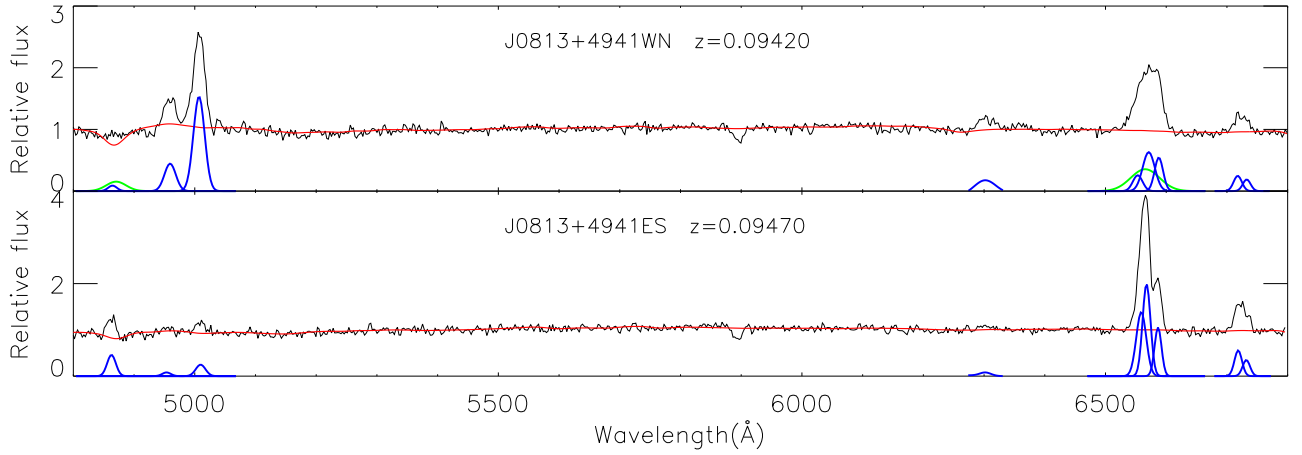


Figure B23. Same as Fig. 3 but for J0813+4941. The spectra from LJT.

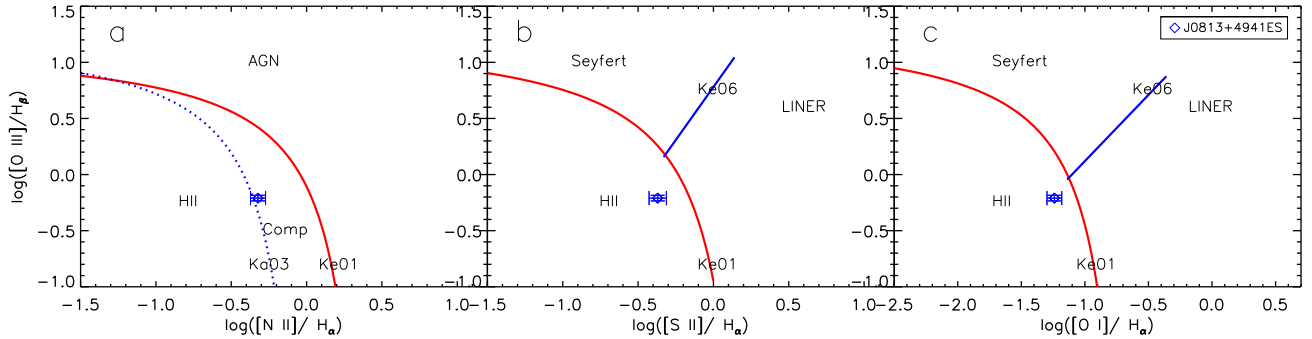


Figure B24. Same as Fig. 5 but for J0813+4941.

DUAL AGN: J081347.49+494109.83

Two sets of AGN spectra are spatially resolved as shown in Fig. B22, so the two cores, i.e. J0813+4941WN and J0813+4941ES can be identified separately.

The fitting of extracted 1D spectra of the two cores are shown in Fig. B23. The redshifts, FWHMs of emission lines and emission line flux ratios of the two cores, measured from the 1D spectra, are presented in Tables 4 and 5. The spectrum of J0813+4941WN has broad line (Fig. B23; $\text{FWHM} > 2000 \text{ km s}^{-1}$ as measured from $\text{H}\alpha$ broad line component) and thus it is a Type I AGN. The spectrum of J0813+4941ES only has narrow line component. We use the BPT diagram to distinguish this AGN shown in Fig. B24 and it is classified as Comp (AGN).

The object J081347.49+494109.83 has been revealed as a dual AGN composed of Type I AGN (J0813+4941WN) and Comp (J0813+4941ES). This dual AGN has a separation of 5.8 kpc and a velocity offset of $150 \pm 40 \text{ km s}^{-1}$.

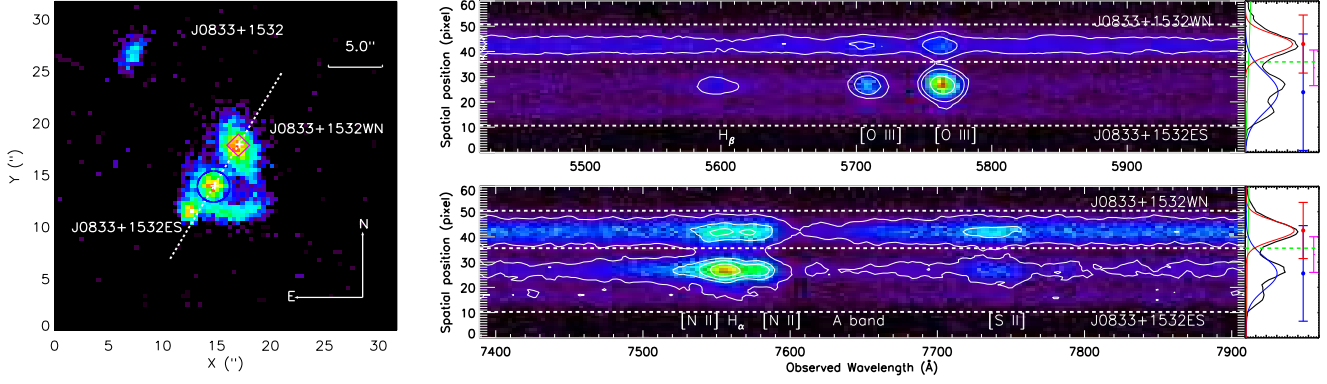


Figure B25. Same as Fig. 1 but for J0833+1532.

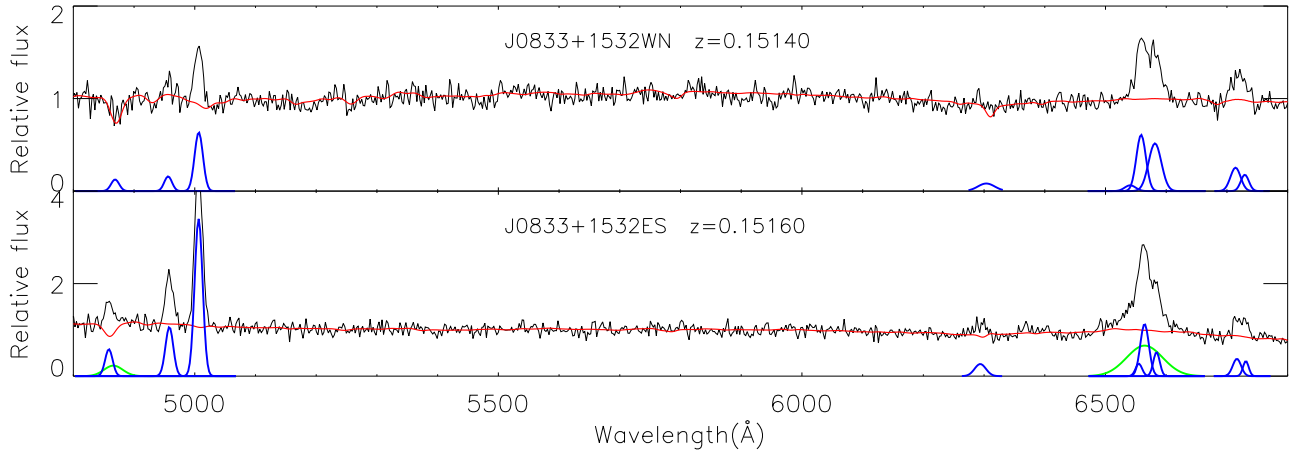


Figure B26. Same as Fig. 3 but for J0833+1532. The spectra from LJT.

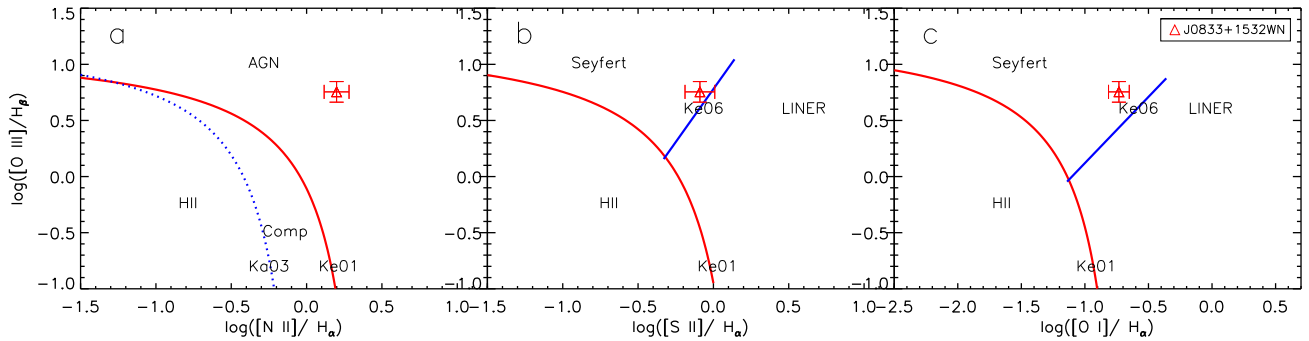


Figure B27. Same as Fig. 5 but for J0833+1532.

DUAL AGN: J083355.49+153236.62

Two sets of AGN spectra are spatially resolved, as shown in Fig. B25, so the two cores, i.e. J0833+1532WN and J0833+1532ES can be identified separately.

The fitting of extracted 1D spectra of the two cores are shown in Fig. B26. The redshifts, FWHMs of emission lines and emission line flux ratios of the two cores, measured from the 1D spectra, are presented in Tables 4 and 5. The spectrum of J0833+1532WN only has narrow line component. We use the BPT diagram to distinguish this AGN shown in Fig. B27 and it is classified as Seyfert (AGN). The spectrum of J0833+1532ES has broad line (Fig. B26; FWHM $> 2000 \text{ km s}^{-1}$ as measured from $H\alpha$ broad line component) and thus it is a Type I AGN.

The object J083355.49+153236.62 has been revealed as a dual AGN composed of Seyfert (J0833+1532WN) and Type I AGN (J0833+1532ES). This dual AGN has a separation of 11.9 kpc and a velocity offset of $60 \pm 40 \text{ km s}^{-1}$.

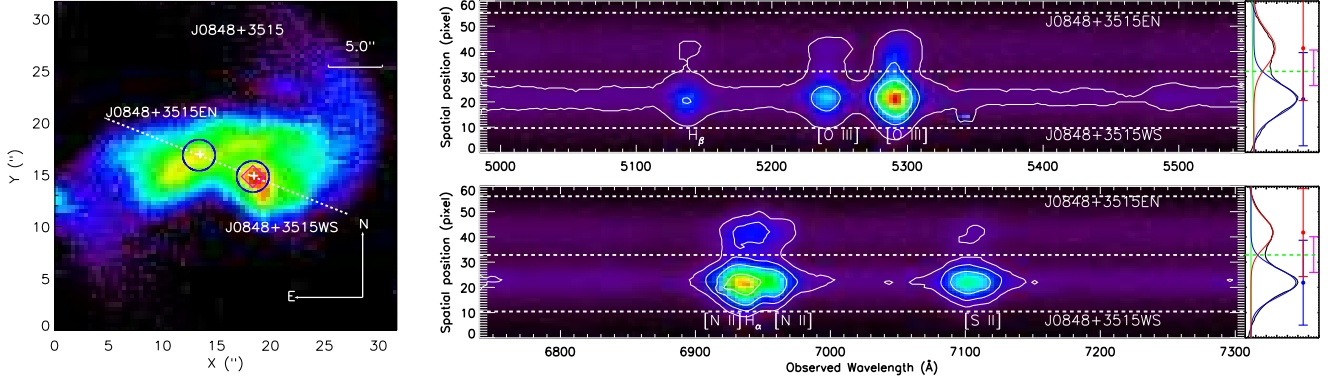


Figure B28. Same as Fig. 1 but for J0848+3515.

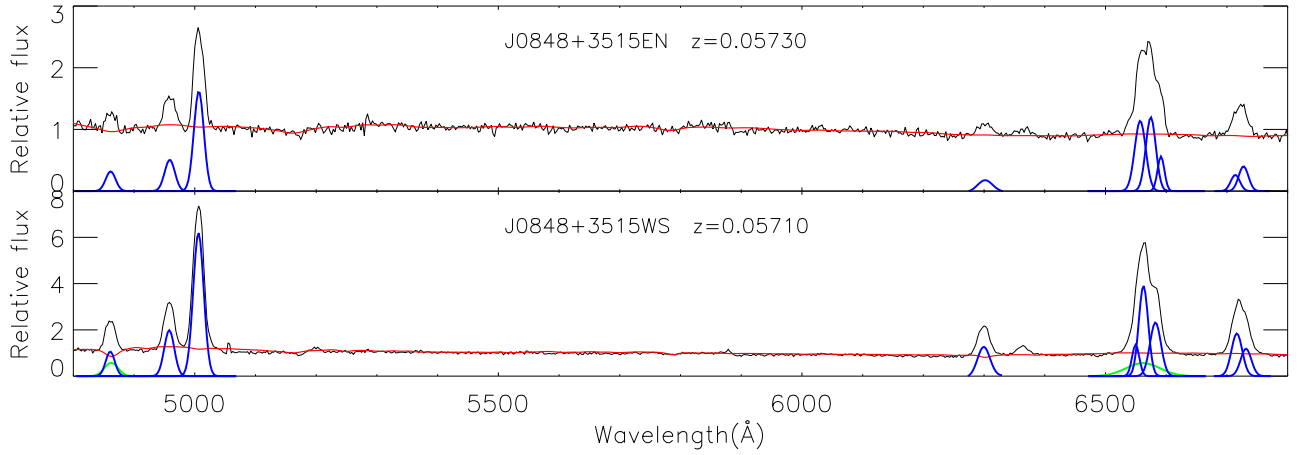


Figure B29. Same as Fig. 3 but for J0848+3515. The spectra from LJT.

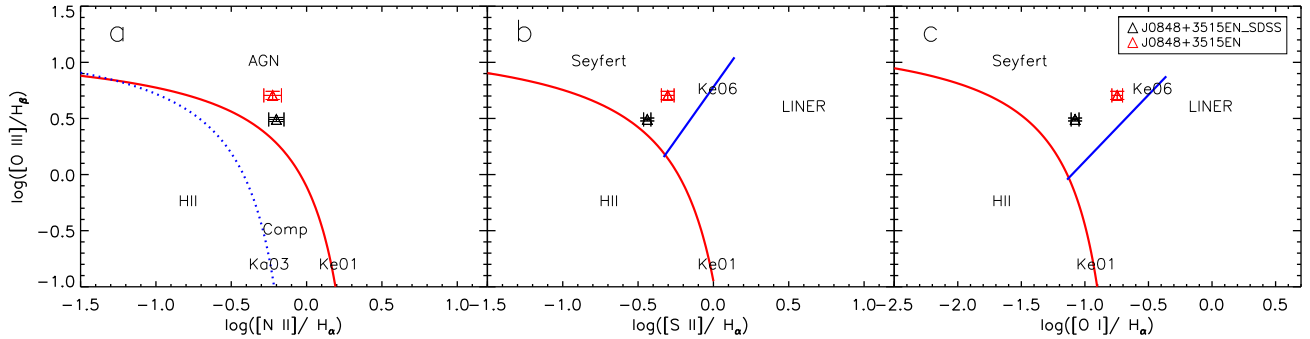


Figure B30. Same as Fig. 5 but for J0848+3515.

DUAL AGN: J084809.69+351532.12

Two sets of AGN spectra are spatially resolved as shown in Fig. B28, so the two cores, i.e. J0848+3515EN and J0848+3515WS can be identified separately.

The fitting of extracted 1D spectra of the two cores are shown in Fig. B29. The redshifts, FWHMs of emission lines and emission line flux ratios of the two cores, measured from the 1D spectra, are presented in Tables 4 and 5. The spectrum of J0848+3515EN only has narrow line component. We use the BPT diagram to distinguish this AGN shown in Fig. B30 and it is classified as Seyfert (AGN). The spectrum of J0848+3515WS has broad line (Fig. B29; FWHM $> 2000 \text{ km s}^{-1}$ as measured from $H\alpha$ broad line component) and thus it is a Type I AGN.

The object J084809.69+351532.12 has been revealed as a dual AGN composed of Seyfert (J0848+3515EN) and Type I AGN (J0848+3515WS). This dual AGN has a separation of 6.2 kpc and a velocity offset of $60 \pm 40 \text{ km s}^{-1}$.

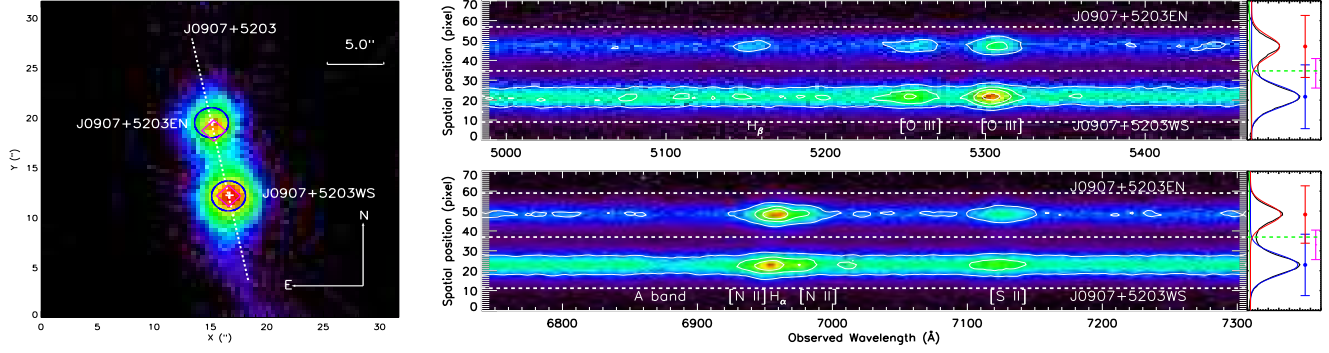


Figure B31. Same as Fig. 1 but for J0907+5203.

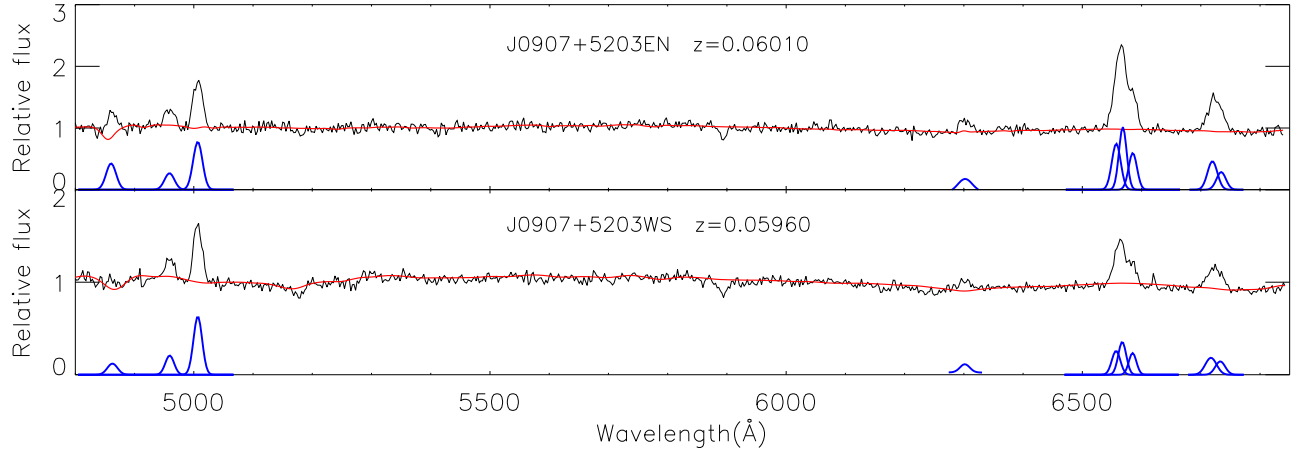


Figure B32. Same as Fig. 3 but for J0907+5203. The spectra from LJT.

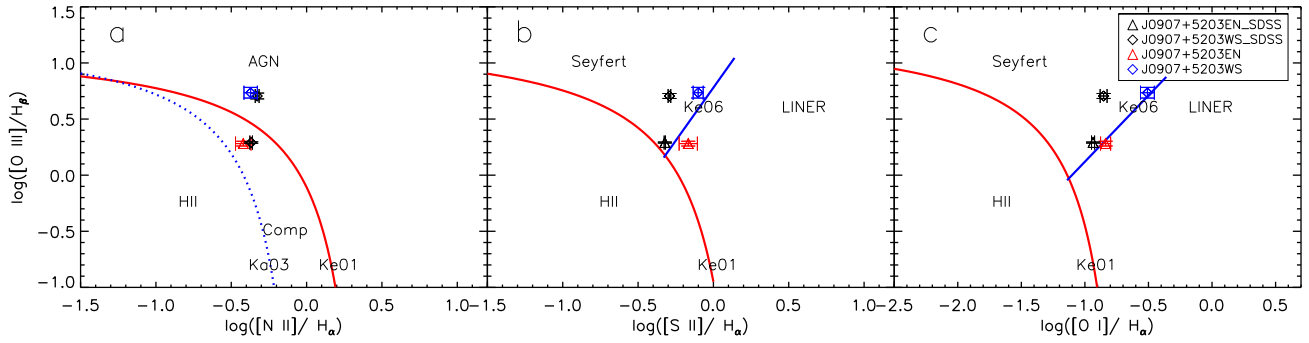


Figure B33. Same as Fig. 5 but for J0907+5203.

DUAL AGN: J090714.61+520350.61

Two sets of AGN spectra are spatially resolved as shown in Fig. B31, so the two cores, i.e. J0907+5203EN and J0907+5203WS can be identified separately.

The fitting of extracted 1D spectra of the two cores are shown in Fig. B32. The redshifts, FWHMs of emission lines and emission line flux ratios of the two cores, measured from the 1D spectra, are presented in Tables 4 and 5. For the two cores, no broad line components are detected, we therefore use BPT diagram to classify their types (Fig. B33). According to the diagnosis, J0907+5203EN is classified as ambiguous AGN and J0907+5203WS is classified as Seyfert (AGN).

The object J090714.61+520350.61 has been revealed as a dual AGN composed of ambiguous galaxy (J0907+5203EN) and Seyfert (J0907+5203WS). This dual AGN has a separation of 8.5 kpc and a velocity offset of $150 \pm 40 \text{ km s}^{-1}$.

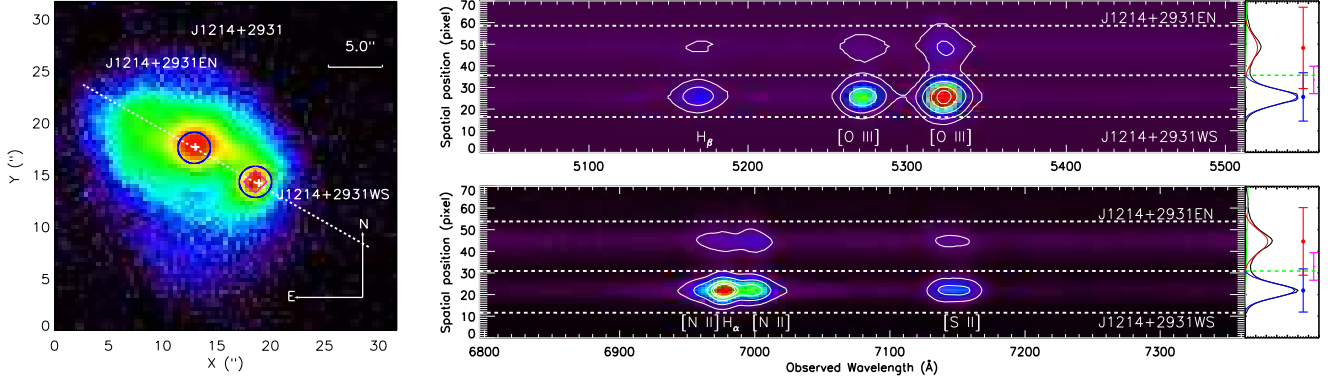


Figure B34. Same as Fig. 1 but for J1214+2931.

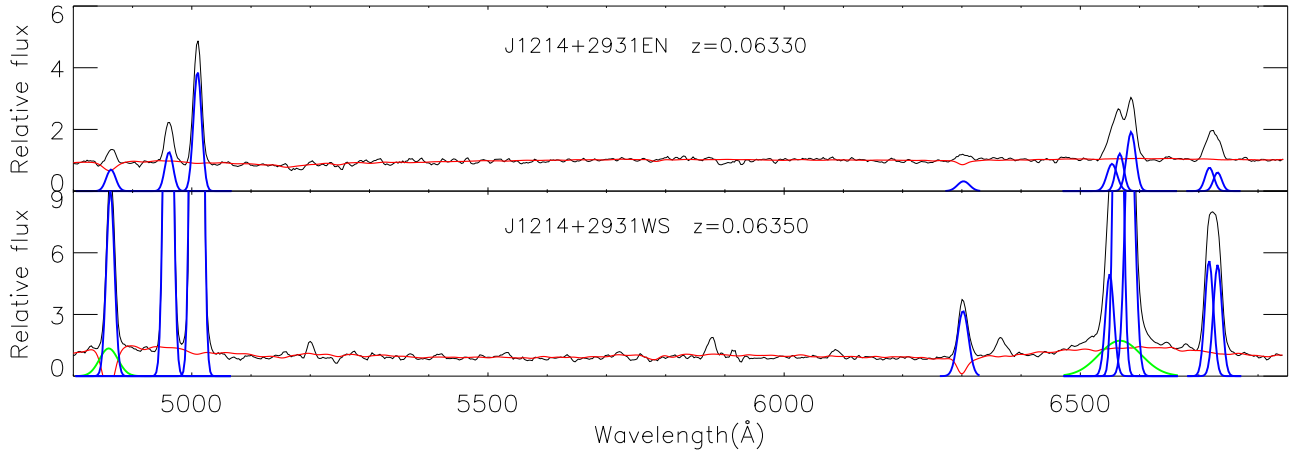


Figure B35. Same as Fig. 3 but for J1214+2931. The spectra from LJT.

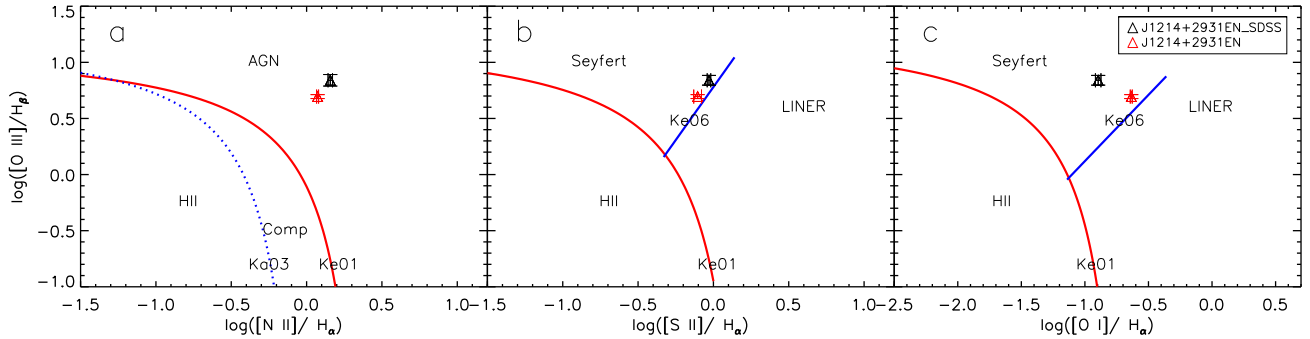


Figure B36. Same as Fig. 5 but for J1214+2931.

DUAL AGN: J121418.25+293146.70

Two sets of AGN spectra are spatially resolved as shown in Fig. B34, so the two cores, i.e. J1214+2931EN and J1214+2931WS can be identified separately.

The fitting of extracted 1D spectra of the two cores are shown in Fig. B35. The redshifts, FWHMs of emission lines and emission line flux ratios of the two cores, measured from the 1D spectra, are presented in Tables 4 and 5. The spectrum of J1214+2931EN only has narrow line component. We use the BPT diagram to distinguish this AGN shown in Fig. B36 and it is classified as Seyfert (AGN). The spectrum of J1214+2931WS has broad line (Fig. B35; $\text{FWHM} > 2000 \text{ km s}^{-1}$ as measured from $\text{H}\alpha$ broad line component) and thus it is a Type I AGN.

The object J121418.25+293146.70 has been revealed as a dual AGN composed of Seyfert (J1214+2931EN) and Type I AGN (J1214+2931WS). This dual AGN has a separation of 9.3 kpc and a velocity offset of $60 \pm 40 \text{ km s}^{-1}$.

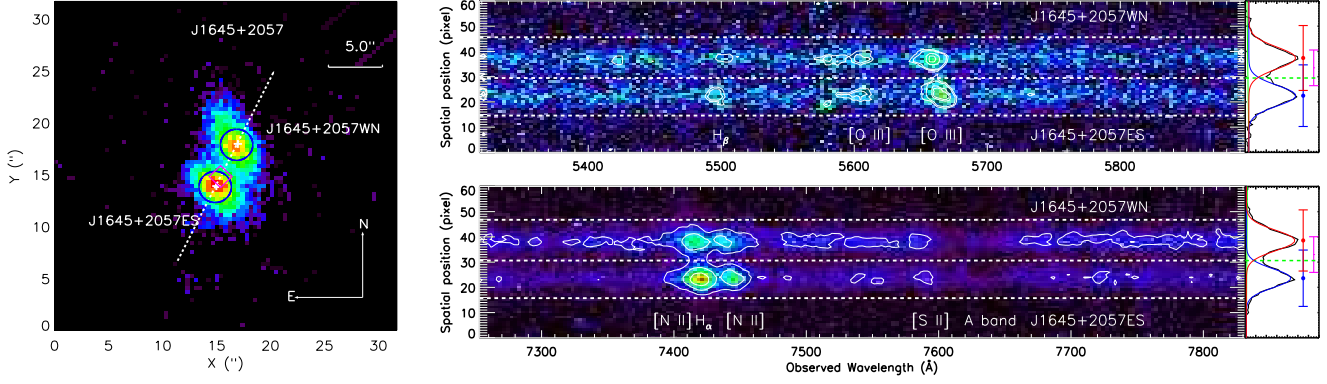


Figure B37. Same as Fig. 1 but for J1645+2057.

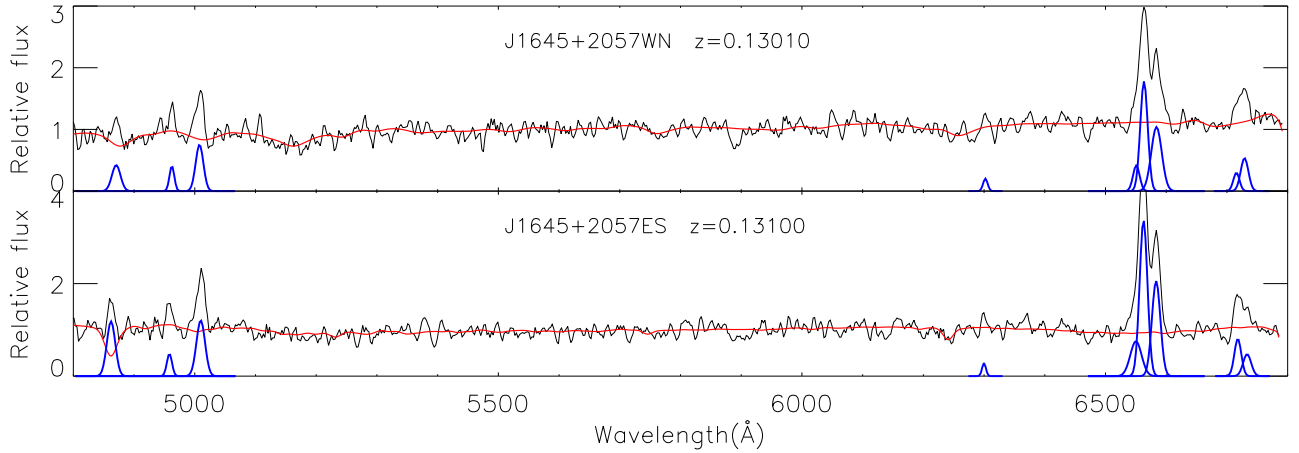


Figure B38. Same as Fig. 3 but for J1645+2057. The spectra from LJT.

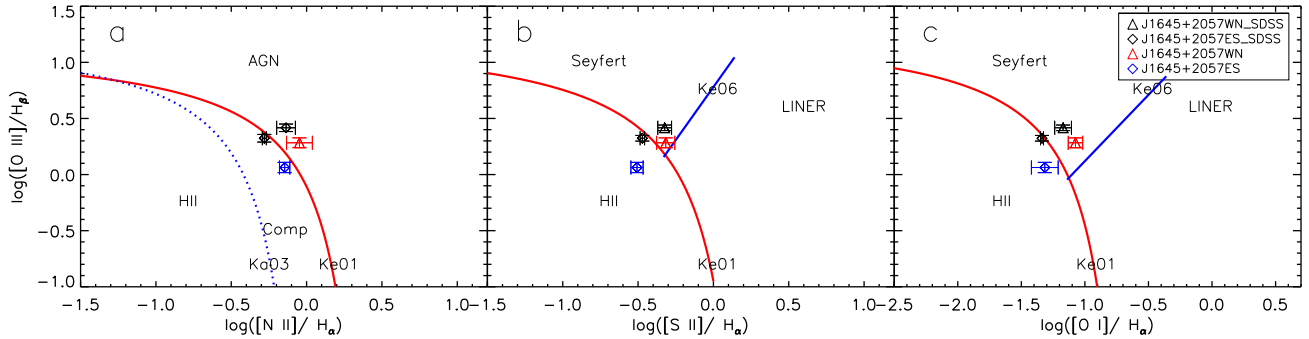


Figure B39. Same as Fig. 5 but for J1645+2057.

DUAL AGN: J164507.91+205759.43

Two sets of AGN spectra are spatially resolved as shown in Fig. B37, so the two cores, i.e. J1645+2057WN and J1645+2057ES can be identified respectively.

The fitting of extracted 1D spectra of the two cores are shown in Fig. B38. The redshifts, FWHMs of emission lines and emission line flux ratios of the two cores, measured from the 1D spectra, are presented in Tables 4 and 5. For the two cores, no broad line components are detected, we therefore use BPT diagram to classify their types (Fig. B39). According to the diagnosis, J1645+2057WN is classified as Seyfert and J1645+2057ES is classified as Comp (AGN).

The object J164507.91+205759.43 has been revealed as a dual AGN composed of Seyfert (J1645+2057WN) and Comp (J1645+2057ES). This dual AGN has a separation of 9.8 kpc and a velocity offset of $270 \pm 40 \text{ km s}^{-1}$.

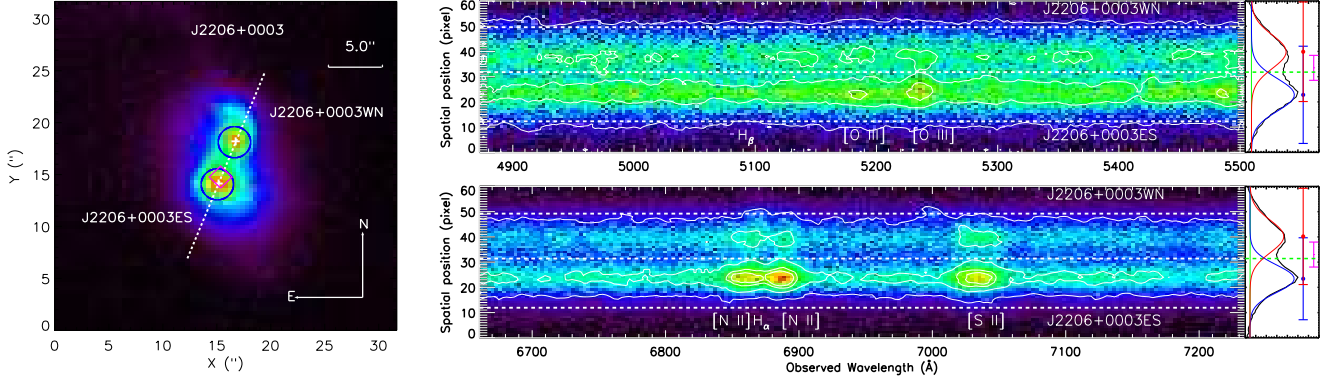


Figure B40. Same as Fig. 1 but for J2206+0003.

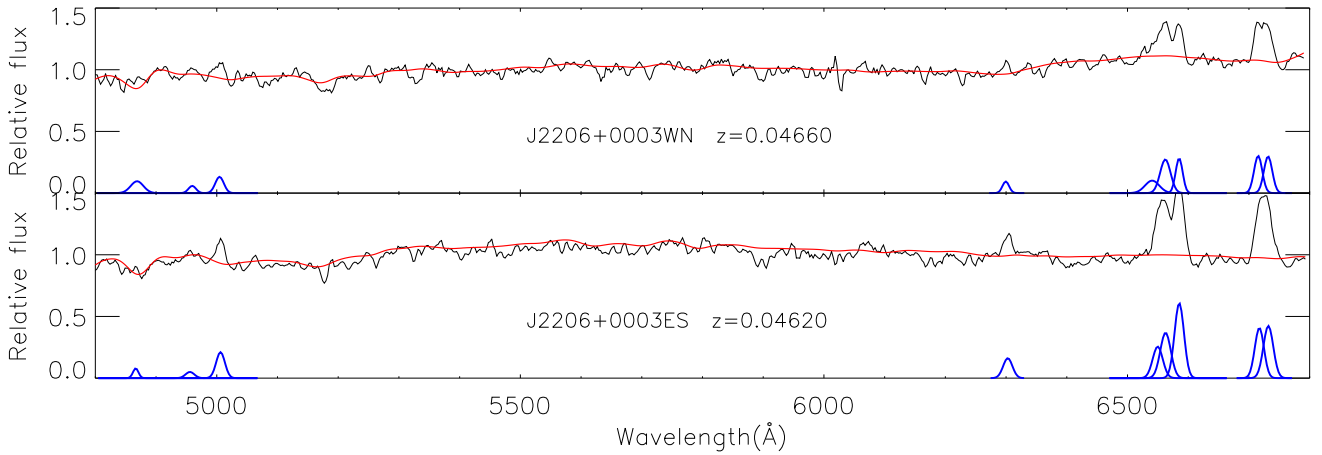


Figure B41. Same as Fig. 3 but for J2206+0003. The spectra from LJT.

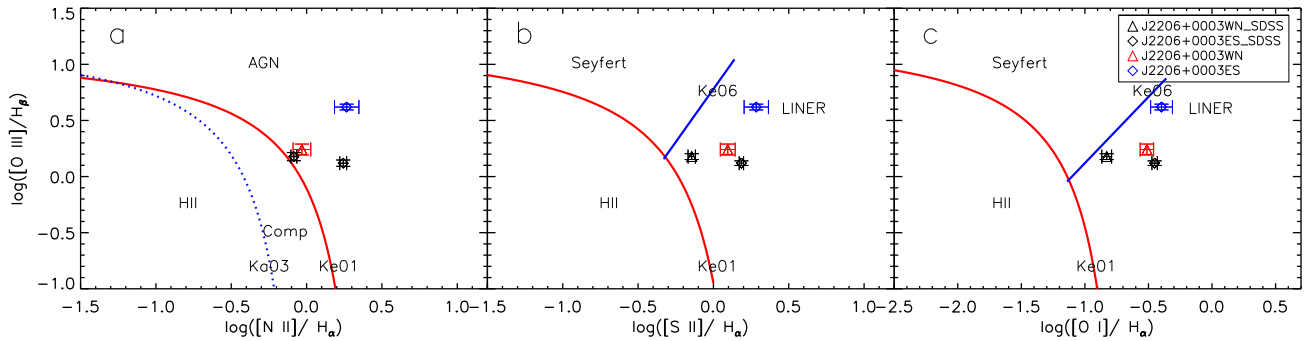


Figure B42. Same as Fig. 5 but for J2206+0003.

DUAL AGN: J220634.97+000327.57

Two sets of AGN spectra are spatially resolved as shown in Fig. B40, so the two cores, i.e. J2206+0003WN and J2206+0003ES can be identified separately.

The fitting of extracted 1D spectra of the two cores are shown in Fig. B41. The redshifts, FWHMs of emission lines and emission line flux ratios of the two cores, measured from the 1D spectra, are presented in Tables 4 and 5. For the two cores, no broad line components are detected, we therefore use BPT diagram to classify their types (Fig. B42). According to the diagnosis, both cores are classified as LINERs (AGN).

The object J220634.97+000327.57 has been revealed as a dual AGN composed of LINER (J2206+0003WN) and LINER (J2206+0003ES). This dual AGN has a separation of 4.3 kpc and a velocity offset of $120 \pm 40 \text{ km s}^{-1}$.

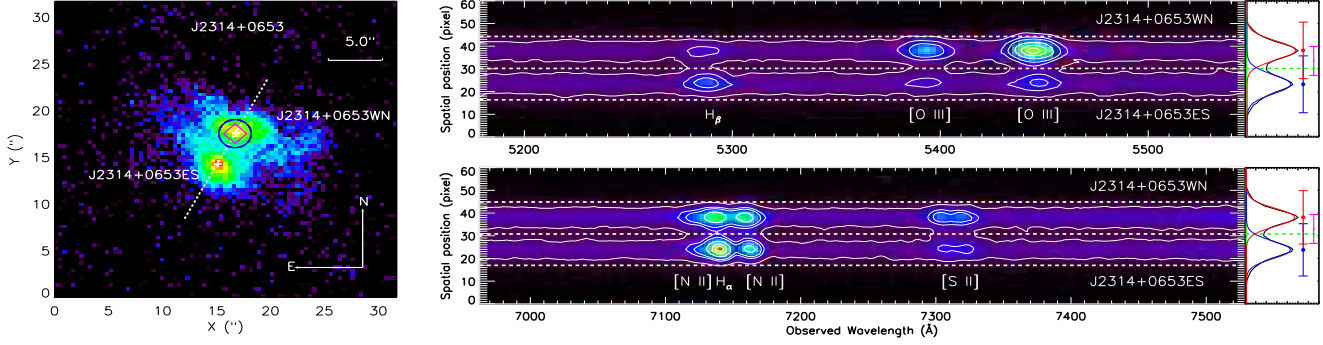


Figure B43. Same as Fig. 1 but for J2314+0653.

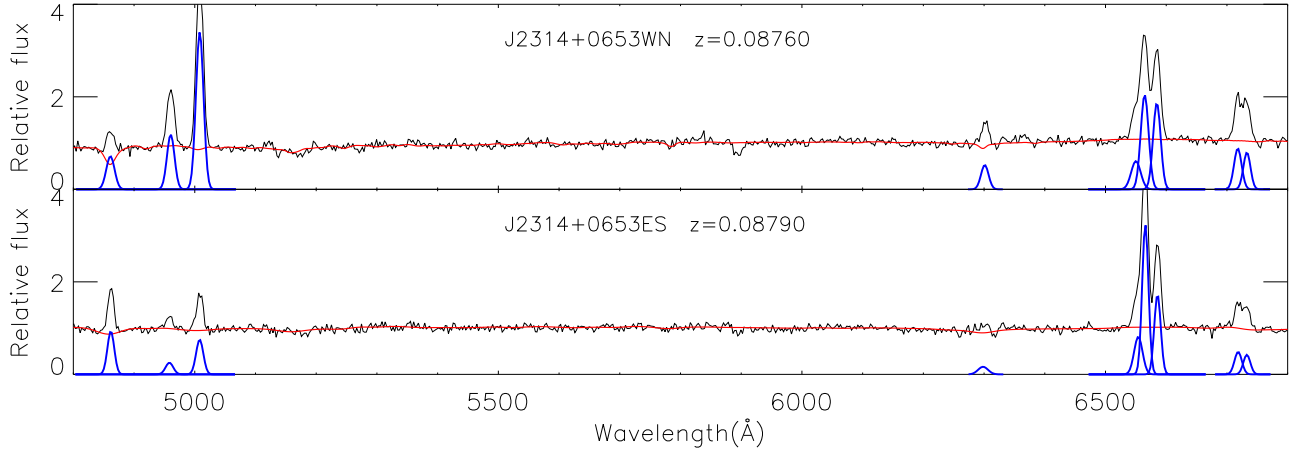


Figure B44. Same as Fig. 3 but for J2314+0653. The spectra from LJT.

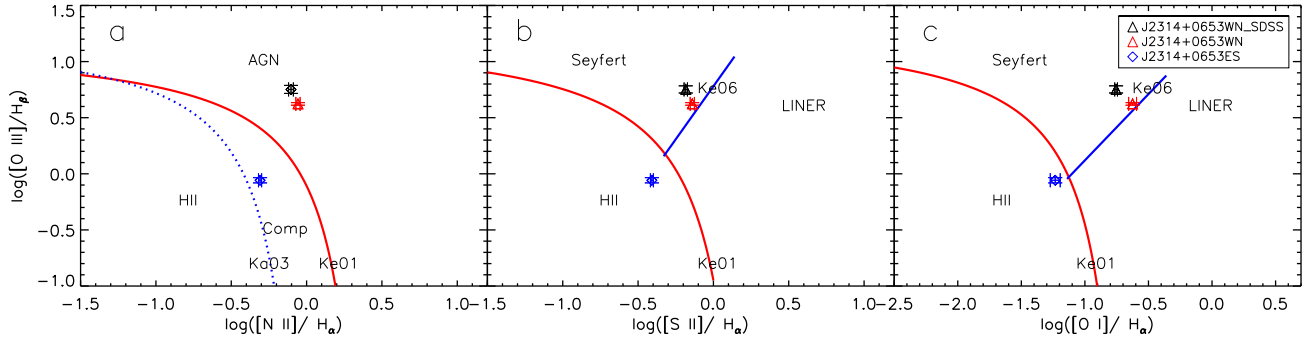


Figure B45. Same as Fig. 5 but for J2314+0653.

DUAL AGN: J231439.21+065312.97

Two sets of AGN spectra are spatially resolved as shown in Fig. B43, so the two cores, i.e. J2314+0653WN and J2314+0653ES can be identified separately.

The fitting of extracted 1D spectra of the two cores are shown in Fig. B44. The redshifts, FWHMs of emission lines and emission line flux ratios of the two cores, are presented in Tables 4 and 5. For the two cores, no broad line components are detected, we therefore use BPT diagram to classify their types (Fig. B45). According to the diagnosis, J2314+0653WN is classified as Seyfert (AGN) and J2314+0653ES is classified as Comp (AGN).

The object J231439.21+065312.97 has been revealed as a dual AGN composed of Seyfert (J2314+0653WN) and LINER (J2314+0653ES). This dual AGN has a separation of 6.7 kpc and a velocity offset of $90 \pm 40 \text{ km s}^{-1}$.